

Brendan F. Kennedy, Kelsey M. Kennedy, Amy L. Oldenburg,  
Steven G. Adie, Stephen A. Boppart, and David D. Sampson

---

## Keywords

Elastography • Optical elastography • Tissue mechanics • Biomechanics •  
Cell mechanics • Soft tissue

---

## 32.1 Introduction

Manual probing (palpation) of a suspicious region is one of the most basic diagnostic tools used by physicians to identify disease. Palpation is sensitive to variations in the mechanical properties (e.g., stiffness) of soft tissue. These properties are determined

---

B.F. Kennedy (✉) • K.M. Kennedy

Optical+Biomedical Engineering Laboratory, School of Electrical, Electronic and Computer Engineering, The University of Western Australia, Crawley, WA, Australia  
e-mail: [Brendan.Kennedy@uwa.edu.au](mailto:Brendan.Kennedy@uwa.edu.au)

A.L. Oldenburg

Department of Physics and Astronomy and the Biomedical Research Imaging Center, University of North Carolina at Chapel Hill, Chapel Hill, NC, USA

S.G. Adie

Department of Biomedical Engineering, Cornell University, Ithaca, NY, USA

S.A. Boppart

Biophotonics Imaging Laboratory, Beckman Institute for Advanced Science and Technology, University of Illinois at Urbana-Champaign, Urbana, IL, USA

Departments of Bioengineering, Electrical and Computer Engineering, and Medicine, University of Illinois at Urbana-Champaign, Urbana, IL, USA

D.D. Sampson

Optical+Biomedical Engineering Laboratory, School of Electrical, Electronic and Computer Engineering, The University of Western Australia, Crawley, WA, Australia

Centre for Microscopy, Characterisation and Analysis, The University of Western Australia, Crawley, WA, Australia

by the composition and organization of the structural components of tissue, including elastin, collagen, and the extracellular matrix and cytoskeletons of cells, as well as its fluid content [1]. Tissue pathologies are accompanied by changes in one or more of these factors, which often leads to a palpable disease state.

Despite its utility, palpation is limited by its subjectivity, low spatial resolution, and poor sensitivity. Over the last 20 years, a diagnostic imaging technique known as elastography has emerged that addresses these issues. In elastography, images (elastograms) are generated based on a tissue's mechanical properties [2]. A range of different approaches has been adopted, generally sharing three key steps.

1. A mechanical load is applied to a tissue.
2. Tissue displacement in response to the load is determined.
3. A mechanical property of tissue is estimated from the measured displacement.

Initially, elastography was developed using ultrasound [3] or magnetic resonance imaging (MRI) [4] as the underlying imaging modalities. A number of pathologies have been targeted, most notably, breast cancer [5], liver fibrosis [6], and prostate cancer [7]. Clinical results have demonstrated improved diagnostic capabilities. For example, in a multicenter study of ultrasound elastography in breast cancer involving more than 750 patients, improved specificity (89.5 %) and positive predictive value (86.6 %) compared with standard ultrasound (76.1 % and 77.2 %) were reported [8]. Both ultrasound and magnetic resonance elastography are commercially available, including from Echosens, General Electric, Hitachi, Philips, Siemens, Supersonic, Toshiba, and Ultrasonix.

The use of optical coherence tomography (OCT) as the underlying imaging modality in elastography, known as optical coherence elastography (OCE), was first demonstrated by Schmitt in 1998 [9]. Closely related optical elastography techniques based on laser speckle imaging [10, 11], ultrasound-modulated optical tomography [12, 13], and digital holography [14, 15] have also been demonstrated. OCE has a number of distinctive aspects in comparison to ultrasound and magnetic resonance elastography or OCT, including.

*Spatial resolution:* OCE has the potential to provide a spatial resolution of 1–10  $\mu\text{m}$ , much higher than for (clinical) ultrasound and MR elastography. Such resolution provides information on length scales not previously studied, with the potential to resolve mechanical heterogeneity in diseases such as cancer.

*Acquisition speed:* OCE provides for 2D image acquisition rates exceeding 1 kHz – generally much higher than for ultrasound or magnetic resonance elastography. Such high speed promises 3D in vivo application without motion artifact.

*Sensitivity:* Sub-nanometer (possibly tens of picometer) displacement sensitivity enables the measurement of smaller changes in mechanical properties than other forms of elastography. This sensitivity has the potential to better differentiate subtle changes, e.g., between benign and malignant tumors.

*Contrast:* The Young's modulus of soft tissue varies from Pa to MPa, whereas the scattering coefficient of such tissues (largely determining contrast in OCT) is typically in the range 2–20  $\text{mm}^{-1}$ . Thus, there is an apparent advantage in the dynamic range of mechanical over optical contrast.

*Imaging penetration:* OCE penetrates only millimeters from the probe, which is much less than for ultrasound and MR elastography. This limitation is overcome by exploiting fiber optics in endoscopic and interstitial probes, which expands the applications of OCE, e.g., to the assessment of atherosclerotic plaques in coronary arteries.

The landscape of OCE is rapidly changing. OCT technology has matured to the point that sub-nanometer displacement sensitivity and rapid image acquisition speeds are enabling, for the first time, the generation of high-resolution, high-contrast elastograms. Commercial and clinical successes in ultrasound and magnetic resonance elastography promise to pave the way for OCE. Current research efforts are focusing on the key advances needed to enable clinical OCE, i.e., quantitative and repeatable measurements, practical imaging probes integrated with loading mechanisms, and convincing demonstrations of contrast in pathological tissue.

In this chapter, we review the basic principles and development of OCE. We begin by describing the mechanical principles of tissue deformation. We then describe how deformation has been measured and review OCE techniques proposed so far. We discuss the development of imaging probes and the fidelity of contrast in elastograms before presenting an outlook for OCE. Throughout, we touch on applications of OCE, which are in their infancy.

---

## 32.2 Tissue Deformation

Fundamentally, elastography is a method for mapping the mechanical properties of tissue from a set of displacement measurements. First, let us consider the physical principles that govern tissue deformation. We use the conventional quantities defined in continuum mechanics to link tissue displacement, deformation, load, and elasticity [16]. We describe the load applied to tissue and the resulting deformation using stress and strain tensors. A constitutive equation is then used to define the elasticity by relating these tensors. In this analysis, we describe tissue as a linearly elastic solid, allowing us to derive a number of elastic properties that characterize its mechanical behavior, including those properties that most closely describe the variations in stiffness that are sensed by manual palpation. It should be recognized that the assumption of linear elasticity is generally not valid for the majority of soft tissues, which are more accurately described as nonlinear viscoelastic materials [1]. However, in elastography, these assumptions are often made to simplify the analysis. Similar analyses have been used to describe tissue deformation in ultrasound and magnetic resonance elastography [17, 18].

### 32.2.1 Stress Tensor

The application of a mechanical load results in stress acting throughout a tissue. To analyze the stress, we consider a volume, subject to an arbitrary number of external forces,  $\mathbf{F}_m$ , as illustrated in Fig. 32.1a. These external forces give rise to internal forces distributed throughout the volume. To define the corresponding

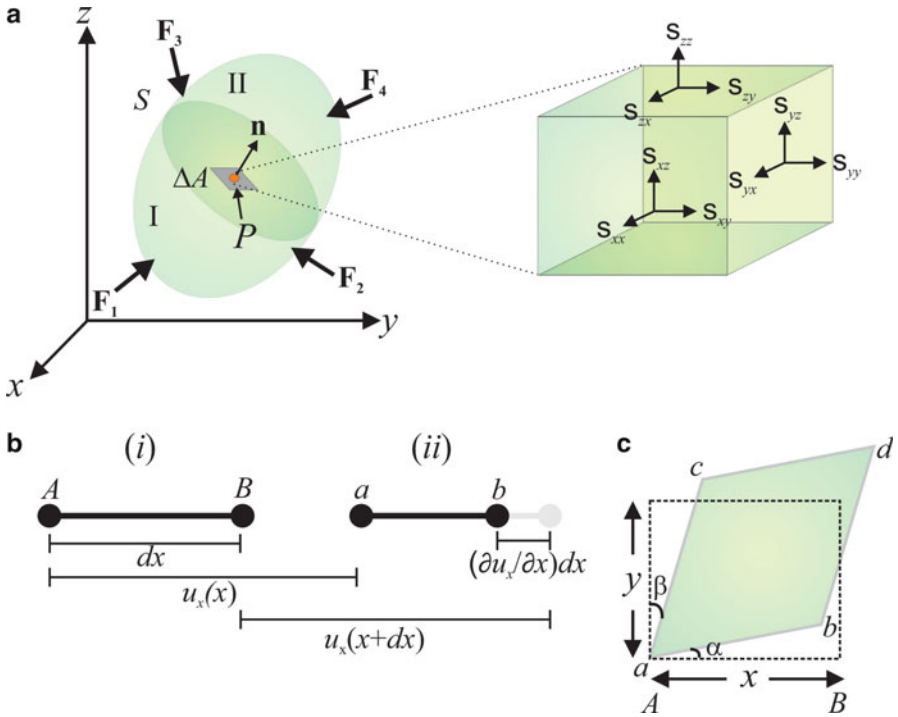


**Fig. 32.1** (a) Stress components acting at the point  $P$  located within a deformable body under load. (b) Normal strain along the  $x$ -axis of the cube in (a) (i) before and (ii) after compressive deformation. The *gray line* in (ii) represents the initial length. (c) Shear strain:  $xy$ -plane of the cube in (a) after shear deformation. The *dashed rectangle* represents the  $xy$ -plane before deformation

stress, we divide the volume into two portions (I and II), using the plane  $S$  which passes through an arbitrary point,  $P$ , with unit normal vector,  $\mathbf{n}$ . Considering I, we assume this portion is in equilibrium under the action of the external forces  $\mathbf{F}_1$  and  $\mathbf{F}_2$  and the internal forces distributed over the plane  $S$  representing the actions of II on I. To obtain the stress acting in the small area  $\Delta A$  in the plane  $S$  containing  $P$ , we assume that the forces acting in this area can be reduced to a resultant force  $\Delta \mathbf{F}$ , where the limiting direction of  $\Delta \mathbf{F}$  is perpendicular to  $S$ . The stress vector,  $\sigma_{\mathbf{n}}$ , acting at this point is defined as

$$\sigma_{\mathbf{n}} = \lim_{\Delta A \rightarrow 0} \frac{\Delta \mathbf{F}}{\Delta A}. \tag{32.1}$$

The S.I. unit of stress is the Pascal, equivalent to  $Nm^{-2}$ . Equation 32.1 defines the particular case where the direction of the resultant force,  $\Delta \mathbf{F}$ , is also the direction of the stress vector. More generally, the direction of the stress vector is inclined to  $\Delta A$  and is described by two components: a normal stress perpendicular

to  $\Delta A$  and a shear stress acting in the plane of  $\Delta A$ . Consider the infinitesimal cubic element located at the point  $P$ , shown in Fig. 32.1a, with faces parallel to the coordinate axes. Each component of stress acting on the cube is highlighted in Fig. 32.1a. Two subscripts are used for each component. The first indicates the direction of the normal to the plane and the second indicates the direction of the stress component. The total stress acting on the cube is described by a second-order tensor:

$$\boldsymbol{\sigma} = \begin{bmatrix} \sigma_{xx} & \sigma_{xy} & \sigma_{xz} \\ \sigma_{yx} & \sigma_{yy} & \sigma_{yz} \\ \sigma_{xz} & \sigma_{yz} & \sigma_{zz} \end{bmatrix}. \quad (32.2)$$

### 32.2.2 Strain Tensor

The strain tensor describes each component of the deformation resulting from an applied load. Consider the  $x$ -axis of the infinitesimal cube presented in Fig. 32.1a. In Fig. 32.1b, this axis is shown (i) before and (ii) after compressive deformation. The component  $u_x$  describes the displacement at the point  $A$ . The initial length along the  $x$ -axis,  $|AB|$ , is given by  $dx$ . After deformation, this length ( $|ab|$  in Fig. 32.1b) is given by  $dx + \frac{\partial u_x}{\partial x} dx$ . The normal strain is defined as the unit elongation/contraction:

$$\varepsilon_{xx} = \frac{|ab| - |AB|}{|AB|} = \frac{\partial u_x}{\partial x}. \quad (32.3)$$

The same analysis holds for the normal strain in the  $y$ - and  $z$ -axes,  $\varepsilon_{yy}$  and  $\varepsilon_{zz}$ , defined as  $\frac{\partial u_y}{\partial y}$  and  $\frac{\partial u_z}{\partial z}$ , respectively. In OCE, the strain defined in Eq. 32.3 is often referred to as the local strain [19]. As the strain is a ratio of lengths, it is dimensionless. By convention, tensile strains are positive and compressive strains are negative. Following this convention, the quantity  $\frac{\partial u_x}{\partial x} dx$  in Fig. 32.1b is negative, and therefore, the compressive strain  $\varepsilon_{xx}$  is also negative. Analogously to stress, the strain has both normal and shear components. The  $xy$ -plane of the cube in Fig. 32.1a is illustrated in Fig. 32.1c. After deformation, the area  $dx dy$  takes the form of a parallelogram in the general case. The shear strain is defined as the change in angle between two axes that were originally orthogonal. From Fig. 32.1c, the shear strain,  $\varepsilon_{xy}$ , is given by  $\alpha + \beta$ . For small displacement gradients, we have  $\alpha = \frac{\partial u_y}{\partial x}$  and  $\beta = \frac{\partial u_x}{\partial y}$ , where  $u_y$  is the displacement along the  $y$ -axis at the point  $A$ , allowing the shear strain,  $\varepsilon_{xy}$ , to be defined as  $\frac{\partial u_y}{\partial x} + \frac{\partial u_x}{\partial y}$ . By interchanging  $x$  and  $y$  and  $u_x$  and  $u_y$ , it can be demonstrated that  $\varepsilon_{xy} = \varepsilon_{yx}$ . Shear strain components in the  $xz$  and  $yz$  planes can be defined in a similar manner. The infinitesimal strain tensor describing each component of strain can then be expressed as

$$\begin{aligned} \varepsilon &= \begin{bmatrix} \varepsilon_{xx} & \varepsilon_{xy} & \varepsilon_{xz} \\ \varepsilon_{yx} & \varepsilon_{yy} & \varepsilon_{yz} \\ \varepsilon_{zx} & \varepsilon_{zy} & \varepsilon_{zz} \end{bmatrix} \\ &= \begin{bmatrix} \frac{\partial u_x}{\partial x} & 0.5 \left( \frac{\partial u_x}{\partial y} + \frac{\partial u_y}{\partial x} \right) & 0.5 \left( \frac{\partial u_x}{\partial z} + \frac{\partial u_z}{\partial x} \right) \\ 0.5 \left( \frac{\partial u_y}{\partial x} + \frac{\partial u_x}{\partial y} \right) & \frac{\partial u_y}{\partial y} & 0.5 \left( \frac{\partial u_y}{\partial z} + \frac{\partial u_z}{\partial y} \right) \\ 0.5 \left( \frac{\partial u_z}{\partial x} + \frac{\partial u_x}{\partial z} \right) & 0.5 \left( \frac{\partial u_z}{\partial y} + \frac{\partial u_y}{\partial z} \right) & \frac{\partial u_z}{\partial z} \end{bmatrix}, \end{aligned} \quad (32.4)$$

where the shear components are scaled by 0.5, as  $\varepsilon_{xy} = \varepsilon_{yx}$ ,  $\varepsilon_{xz} = \varepsilon_{zx}$ , and  $\varepsilon_{yz} = \varepsilon_{zy}$ . It should also be noted that in dynamic elastography techniques, the strain rate is often measured. Strain rate is defined as the rate of change of strain with time [1] and is easily obtained from the expressions defined in Eq. 32.4.

### 32.2.3 Constitutive Equation for a Linearly Elastic Solid

Having defined the load applied to tissue using the stress tensor and the resulting deformation using the strain tensor, a constitutive equation relating the two is used to define tissue elasticity. In elastography, the most commonly used constitutive equation is that of a linearly elastic (or Hookean) solid in which the relationship between stress and strain is linear and strain is independent of the rate at which the load is applied. The constitutive equation for a linearly elastic solid is

$$\sigma_{ij} = C_{ijkl}\varepsilon_{kl}, \quad (32.5)$$

where  $i, j, k$ , and  $l$  define each tensor component. As  $\sigma$  and  $\varepsilon$  are second-order tensors,  $C$  is a fourth-order tensor, consisting of 81 elastic constants, referred to as the elasticity tensor. To simplify the analysis, it is frequently assumed that the elasticity is isotropic, i.e., elasticity can be described without reference to direction. This imposes maximum symmetry on the tensor, reducing the 81 elastic constants to two and resulting in the isotropic linear elastic constitutive equation, defined as

$$\sigma_{ij} = \lambda\varepsilon_{kk}\delta_{ij} + 2\mu\varepsilon_{ij}, \quad (32.6)$$

where  $\lambda$  and  $\mu$  are the elastic constants, also known as the Lamé constants, and  $\delta_{ij}$  is the Kronecker delta (equal to 1 if  $i = j$  and 0 otherwise). As  $\varepsilon$  is dimensionless, the unit for  $\lambda$  and  $\mu$  is that of stress, i.e., the Pascal. It should be noted that constitutive equations that more accurately model the nonlinear viscoelastic response of soft

tissue to loading have also been proposed [20]. However, their complexity has restricted their use in OCE.

### 32.2.4 Elastic Properties

A number of descriptors may be derived from the Lamé constants for a material's elastic properties. In this section, we define these descriptors, namely, Young's modulus, shear modulus, bulk modulus, and Poisson's ratio and describe their relevance to OCE.

*Young's modulus*,  $E$ , characterizes the elasticity of a material subjected to uniaxial stress, i.e., only one normal stress component in Eq. 32.2 is nonzero. Uniaxial stress is generally a good approximation for the loads applied in OCE. For a load acting along  $z$ ,  $E$  is defined as  $\sigma_{zz}/\varepsilon_{zz}$ , i.e., the ratio of normal (axial) stress to normal (axial) strain. In terms of the Lamé constants, it is expressed as  $\frac{\mu(3\lambda+2\mu)}{(\lambda+\mu)}$ .  $E$  has the same unit as stress, i.e., the Pascal.

*Shear modulus*,  $G$ , is the ratio of shear stress to shear strain, e.g.,  $\sigma_{xz}/\varepsilon_{xz}$ . It is equal to the Lamé constant,  $\mu$ , and its unit is the Pascal.

*Bulk modulus*,  $K$ , is defined as the ratio of hydrostatic pressure,  $\sigma$ , to unit volume change,  $\Delta v/v$ . Hydrostatic pressure describes the situation when all shear stress components are zero and the normal stress components are equal, i.e.,  $\sigma_{xx} = \sigma_{yy} = \sigma_{zz}$ .  $K$  is a measure of the compressibility of a material and defined as  $\lambda + \frac{2}{3}\mu$ , and its unit is the Pascal. Its unit of measurement is the Pascal.

*Poisson's ratio*,  $\nu$ , is defined as the ratio of the normal strain along the axis of stress to the normal strain in each orthogonal axis. In compression, it is the ratio of elongation per unit breadth to contraction per unit length, e.g.,  $-\varepsilon_{xx}/\varepsilon_{zz}$ , where the negative sign results from the division of a tensile normal strain,  $\varepsilon_{xx}$ , by a compressive normal strain,  $\varepsilon_{zz}$ . It is defined in terms of the Lamé constants as  $\frac{\lambda}{2(\lambda+\mu)}$ . As it is a ratio of two strains, it is dimensionless.

The Lamé constants, Young's modulus, shear modulus, bulk modulus, and Poisson's ratio are related. Only two of these parameters are independent for an isotropic, linearly elastic material, and thus, measurement of any two determines the other parameters. For soft tissue, the high water content results in the near conservation of volume upon compression. As a result, the bulk modulus of soft tissue has been reported to vary by less than 15 % from that of water [17]. The incompressibility of soft tissue also results in a Poisson's ratio of very close to but not exceeding 0.5. As these properties do not vary significantly for soft tissues, the goal of most OCE techniques is to estimate Young's modulus or shear modulus, which has a much larger dynamic range. These moduli also correspond most closely to what is sensed by manual palpation of the tissue. In soft tissue, it is readily shown that  $E \approx 3G$ , under the assumption that  $\nu \approx 0.5$  [16]. Therefore, Young's modulus is the most common single property used to characterize tissue elasticity and the most commonly probed property in OCE. The value of Young's

modulus of soft tissues extends from tens of Pascals, in very soft tissues such as adipose [21], to hundreds of kPa to MPa, as in hard tumors [22].

### 32.2.5 Equations of Motion

In some OCE techniques, as well as in some ultrasound and magnetic resonance elastography techniques, a dynamic (sinusoidal) load is applied to the sample. In this case, inertia must be taken into account. The constitutive equation of motion for a linearly elastic solid is given by Navier's equation as [16]

$$\rho_0 \frac{\partial^2 \mathbf{u}}{\partial t^2} = (\lambda + \mu) \nabla (\nabla \cdot \mathbf{u}) + \mu \nabla^2 \mathbf{u}, \quad (32.7)$$

where  $\rho$  is the density of the tissue and  $\mathbf{u}$  is the displacement vector. Transverse and longitudinal waves can propagate independently in the material: S (shear) waves and P (pressure) waves, respectively. For shear wave propagation, there is no volume change in the material. The dilatation term ( $\nabla \cdot \mathbf{u}$ ) is therefore zero and Eq. 32.7 becomes

$$\nabla^2 \mathbf{u} = \frac{1}{c_s^2} (\lambda + \mu) \nabla (\nabla \cdot \mathbf{u}) + \mu \nabla^2 \mathbf{u}, \quad (32.8)$$

where  $c_s$ , the shear wave speed, is defined as  $\sqrt{\mu/\rho}$ . Pressure waves are irrotational, i.e.,  $\nabla \times \mathbf{u} = 0$ , allowing  $\mathbf{u}$  to be written in terms of a potential,  $\psi$ , such that  $\mathbf{u} = \nabla \psi$ . The wave equation then becomes

$$\nabla^2 (\nabla \psi) = \frac{1}{c_p^2} (\lambda + \mu) \nabla (\nabla \cdot \mathbf{u}) + \mu \nabla^2 \mathbf{u}, \quad (32.9)$$

where the P-wave speed,  $c_p$ , is defined as  $\sqrt{\frac{\lambda+2\mu}{\rho}}$ .

For soft tissues, the pressure wave speed, typically several thousand m/s, is orders of magnitude faster than the shear wave speed, typically several m/s [18]. The focus in dynamic OCE to date has mainly been to measure elasticity from the shear wave properties [23–26]. There are several reasons for this: firstly, as the P-wave speed depends on variations of the bulk modulus, it has a much lower dynamic range in tissue than S-waves; secondly, the high speed of P-waves makes their detection challenging.

An advantage of dynamic OCE is that it should enable the complex dynamic mechanical response of a sample to be measured, providing information about both its elastic and viscoelastic properties. OCE techniques that have been used to measure viscoelastic properties of tissue are discussed in more detail in Sect. 32.4.4. Dynamic OCE is also potentially more suitable for in vivo measurements, as it enables loading in a frequency range not affected by sample motion, e.g., due to breathing.

## 32.3 Measuring Displacement in OCE

The accuracy and dynamic range of the displacement measured in response to a load has a major impact on elastogram quality. In this section, we describe three techniques to measure the displacement: speckle tracking, phase-sensitive detection, and use of the Doppler spectrum.

### 32.3.1 Speckle Tracking

Speckle is the phenomenon of fine-scale, apparently random, fluctuating light and dark intensity present in all coherent imaging systems. In OCT, it is generated by the summation of the multiple backscattered optical wavefields arising from the sub-resolution sample scatterers. The wavefields may be represented as a summation of complex phasors, which determines the intensity and phase of the detected signal. A detailed analysis of OCT speckle can be found elsewhere [27].

Speckle tracking may be considered to be a sub-branch of the much broader field of speckle metrology, developed since the late 1960s [28, 29]. The utility of speckle for tracking motion in OCE arises because each speckle realization, far from being random, is dependent upon the precise location of backscatterers within the sample. As the backscatterers translate, within a certain range, so does the speckle pattern associated with them. Under the assumption that the relative positions of sub-resolution scatterers remain fixed while they translate, any variation of the speckle pattern between successive acquisitions, or equivalently, of its second-order temporal statistics, can be used to measure sample motion. This is shown in Fig. 32.2, in which a small portion of an OCT speckle pattern acquired from a homogeneously scattering phantom under compressive load (applied from above) is shown in false color. The pattern is shown for four increments in load, increasing from Fig. 32.2a–d. Translation of a single bright speckle is highlighted by a black outline in each figure part. Evident in Fig. 32.2 is the gradual decorrelation of the speckle pattern with load, a major limitation of the technique. This decorrelation is caused by the reorganization of the positions of the sub-resolution scatterers due to loading. It limits the maximum measurable displacement to considerably less than the OCT resolution.

The speckle shift is typically evaluated by calculating the cross-correlation of a portion of B-scans acquired at two time points during compression [9]. Consider a point scatterer embedded in a transparent medium at position  $(x, z)$ . When the sample is placed under load, the scatterer is displaced to a new location,  $(x + \Delta x, z + \Delta z)$ . The normalized cross-correlation between the OCT signal before,  $I_1(x, z)$ , and after loading,  $I_2(x, z)$ , within a predefined window of dimensions  $X \times Z$ , is given by

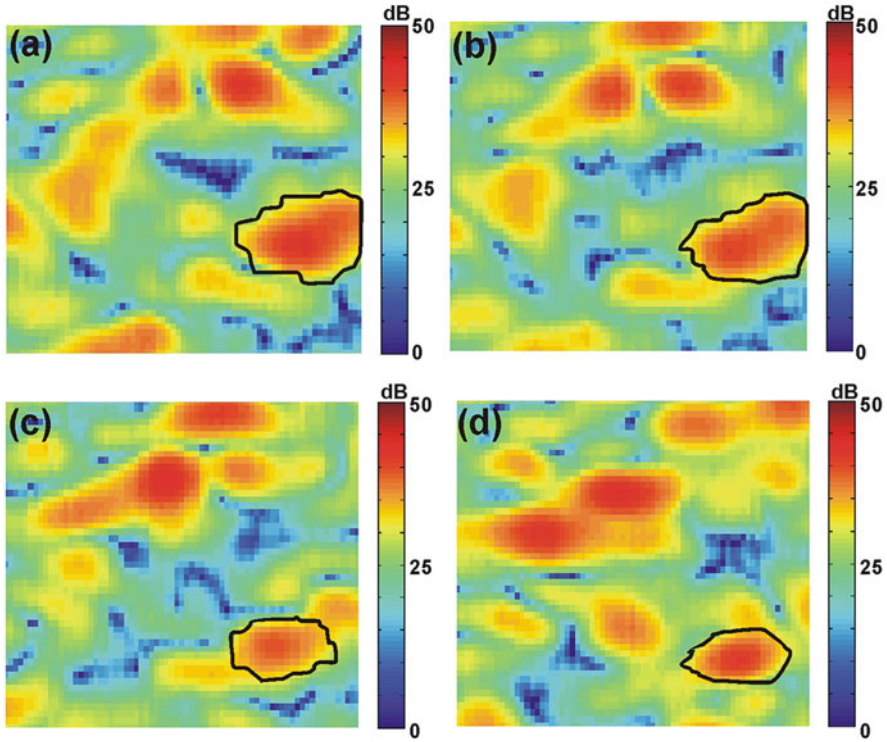


**Fig. 32.2** Speckle pattern of a silicone phantom (logarithmic intensity scale) under increasing compressive load (applied from above) from (a–d). Image dimensions  $50 \times 50 \mu\text{m}$ . Black outline highlights the evolution of an individual speckle

$$\rho(x', z') = \frac{\int_{-Z/2}^{Z/2} \int_{-X/2}^{X/2} I_1(x, z) I_2(x - x', z - z') dx dz}{\sqrt{\int_{-Z/2}^{Z/2} \int_{-X/2}^{X/2} I_1^2(x, z) dx dz \int_{-Z/2}^{Z/2} \int_{-X/2}^{X/2} I_2^2(x - x', z - z') dx dz}}. \quad (32.10)$$

The relative displacement, between the acquisition of  $I_1(x, z)$  and  $I_2(x, z)$ , in the  $x$  and  $z$  directions can then be determined from

$$\Delta u_x = \max[(\rho(x', z'))] \text{ for } z' = 0, -X/2 \leq x' \leq X/2, \quad (32.11)$$

and

$$\Delta u_z = \max[(\rho(x', z'))] \text{ for } x' = 0, -Z/2 \leq z' \leq Z/2. \quad (32.12)$$

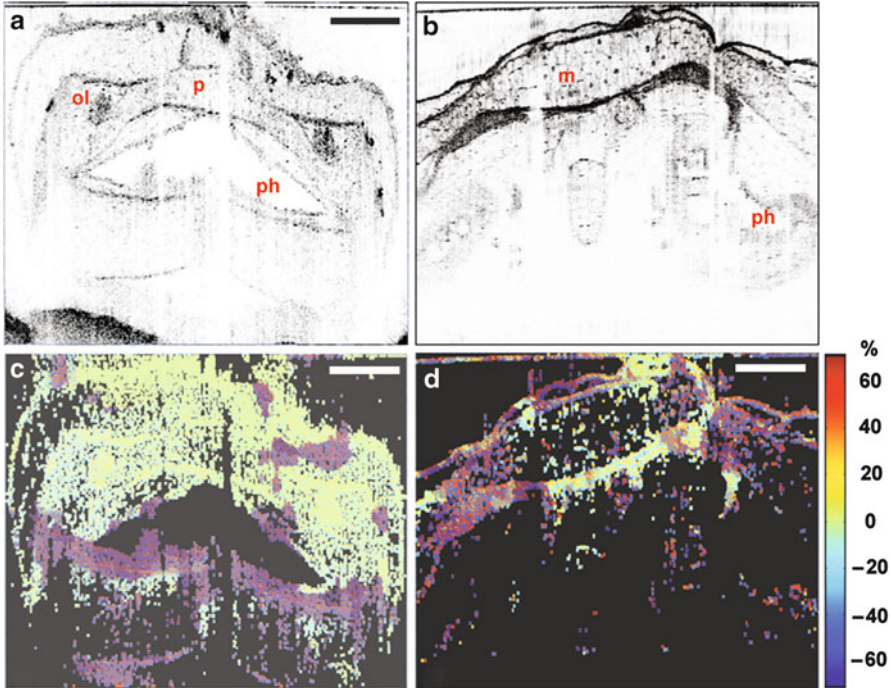


**Fig. 32.3** OCT images and strain maps of a *Xenopus laevis* tadpole at different life cycle stages. (a, c) Representative structural OCT and OCE relative (local) strain maps, respectively, for stage 42 (3 -day-old). (b, d) Representative structural OCT and OCE relative (local) strain maps for Stage 50 (15 -day-old). Scale bar = 300  $\mu\text{m}$  (adapted from [34])

From Eqs. 32.10–32.12,  $\rho$  is maximum for  $x' = \Delta x$  and  $z' = \Delta z$ , respectively. Correlation-based speckle tracking was used in early OCE research [9, 30–34] and has been commonly used in ultrasound elastography [3]. Early examples of OCE elastograms obtained using correlation-based speckle tracking, along with the corresponding OCT images, acquired from a *Xenopus laevis* tadpole at different stages of development are shown in Fig. 32.3.

The minimum measurable displacement obtainable with speckle tracking is determined by the spatial sampling in the underlying OCT system, assuming an adequate OCT SNR. For cross-correlation techniques that use a central difference approach to evaluate Eq. 32.10, this corresponds to 0.5 pixels [10]. Displacements as small as 0.1 pixels can be measured using parametric techniques, such as the maximum likelihood estimator [11, 35]. However, these estimators result in intolerably large errors for displacements  $>0.8$  pixels.

The maximum measurable displacement using the cross-correlation method is set by speckle decorrelation, as mentioned, which depends on the sample elasticity as well as on the size range, density, and arrangement of the sub-resolution scatterers. In a study on a silicone phantom containing titanium dioxide particles,

the maximum displacement was reported to be  $\sim 0.5$  times the resolution of the OCT system [35]. Low OCT SNR also results in decorrelation between successive B-scans [35], reducing the accuracy of displacement measurements with increasing depth in the sample.

The above limits imply a severely limited dynamic range for speckle tracking. Consider an OCT system with spatial resolution of  $10 \times 10 \times 10 \mu\text{m}$  and spatial sampling such that the axial pixel size is  $3 \mu\text{m}$  and the lateral pixel size is  $1 \mu\text{m}$ . Use of a smaller pixel size either imposes restrictions on the field of view (for fixed pixel count) or increases in the acquisition time (for more pixels). Using cross-correlation, minimum and maximum measurable displacements of  $\sim 1.5$  and  $\sim 5 \mu\text{m}$  (from the example in [36]), respectively, might be reasonably expected and correspond to a dynamic range of  $\sim 3.3$ , with the same range applying to the measurable elasticity in OCE.

An additional limitation is that the displacement is calculated within a predefined window ( $X \times Z$  in Eq. 32.10). The window sets the imaging spatial resolution of each displacement measurement, lowering it relative to the OCT image resolution, typically by a factor of 5–10 [9, 31].

An important further consideration when using speckle tracking is the avoidance of decorrelation caused by changes in the tissue configuration not related to its elastic properties, such as bulk motion, Brownian motion, or blood flow. This implies an acquisition speed high enough to ensure the speckles remain correlated between successive scans.

An advantage of speckle tracking is that motion can be tracked in more than one spatial dimension. Speckle tracking in OCE has been performed in only one or two dimensions, but 3D tracking has been proposed in ultrasound [37]. 3D tracking would provide the opportunity to measure shear strain in addition to normal strain (see Eq. 32.4) and to remove the otherwise necessary assumption of isotropic mechanical behavior. This may provide additional OCE contrast in anisotropic tissues, such as skin and muscle, as has already been demonstrated in ultrasound [38] and magnetic resonance elastography [39]. Indeed, 3D information is routinely obtained in magnetic resonance elastography.

### 32.3.2 Phase-Sensitive Detection

Speckle tracking utilizes changes in the *intensity* of an OCT image with loading. In Fourier-domain (FD) OCT, after performing a Fourier transform on the detected spectral fringes, the depth-resolved complex signal is obtained. This provides the opportunity to analyze the *phase* of the detected signal. OCT phase is generally random in soft tissue; however, it is temporally invariant if the sample is stationary. If a sample is subjected to mechanical loading, its axial displacement,  $\Delta u_z$ , between two A-scans, acquired from the same lateral position, results in a phase shift,  $\Delta\phi$  [40]. The displacement,  $\Delta u_z$ , along the axis of the incident beam is defined as

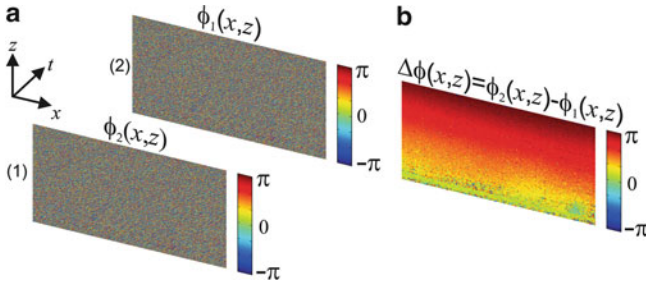


**Fig. 32.4** Schematic illustration of phase-sensitive detection with experimental data from a mechanically homogeneous silicone phantom. **(a)** The phase of OCT B-scans acquired at the same lateral position before (1) and after (2) sample loading. **(b)** Phase difference between the B-scans shown in **(a)**. As the load was applied from the *top*, the phase difference is maximum in this position, reducing to near zero at large depths

$$\Delta u_z(z, t) = \frac{\Delta\phi(z, t)\lambda}{4\pi n}, \quad (32.13)$$

where  $\lambda$  is the mean wavelength of the source and  $n$  is the average refractive index along the beam path. The phase difference is calculated either between two successive A-scans in a B-scan (requiring high lateral sampling density) [40] or between two A-scans acquired in the same lateral position in successive B-scans [41]: the latter is illustrated in Fig. 32.4 with experimental data acquired from a uniformly scattering silicone phantom. Phase-sensitive detection was initially developed for Doppler flow velocity measurement in OCT [42]. Indeed, the phase-sensitive technique is based on the Doppler shift; thus, unlike speckle tracking, only the axial component of the displacement can be detected. If we assume that the maximum measurable displacement is set by the maximum unambiguous phase difference, i.e.,  $2\pi$ , then this corresponds to half the source center wavelength (in the sample medium). The minimum measurable displacement,  $\sigma_{\Delta u_z}$ , is determined by the phase sensitivity of the OCT system [43], which, in the shot-noise limited regime, is related to the OCT signal-to-noise ratio (SNR) and is approximated as

$$\sigma_{\Delta\phi} = \frac{1}{\sqrt{SNR}}, \quad SNR \gg 1. \quad (32.14)$$

Park et al., in their work on flow imaging [44], demonstrated good agreement between Eq. 32.14 and experimental results for OCT SNR > 30 dB. It is important to emphasize, however, that this approximation is only valid for large OCT SNR.

Another source of phase noise is introduced under the successive A-scans scenario if the temporally displaced beams are not precisely overlapped in space. The phase noise introduced due to lateral beam motion,  $\Delta x$ , between successive A-scans is given by [44]

$$\sigma_{\Delta x} = \sqrt{\frac{4}{3} \left\{ 1 - \exp \left[ -2 \left( \frac{\Delta x}{w} \right)^2 \right] \right\}}, \quad (32.15)$$

where  $w$  is the  $1/e^2$  beam width at the focus. In practice, to minimize phase noise due to scanning, dense sampling is performed along the axis used to calculate the phase difference. As an example, consider a typical OCT system with a  $1/e^2$  beam width of 25  $\mu\text{m}$  at the focus. Acquiring A-scans in 1  $\mu\text{m}$  lateral steps ensures that the phase noise due to scanning is  $<0.05$  rad, within a factor of 5 of the limiting phase noise for OCT SNR = 40 dB. A further source of phase noise,  $\sigma_{mech}$ , is introduced by mechanical instabilities in the system, such as jitter in the scanning mirrors. Combining Eqs. 32.14 and 32.15 and including mechanical instabilities, considering each of these processes to be additive and Gaussian, the total phase noise,  $\sigma_{Tot}$ , is given by

$$\sigma_{Tot} = \sqrt{\sigma_{\Delta\phi}^2 + \sigma_{\Delta x}^2 + \sigma_{mech}^2}. \quad (32.16)$$

To minimize  $\sigma_{Tot}$ , both  $\sigma_{\Delta\phi}$  and  $\sigma_{mech}$  must be negligible and the OCT SNR must be maximized (see Eq. 32.14). Under these conditions, displacement sensitivity of  $\sim 20$  pm has been reported [45]. The minimization of  $\sigma_{mech}$  has been discussed in detail in relation to optical coherence microscopy (see ► Chap. 28, “Optical Coherence Microscopy” for more details). Techniques employed to minimize  $\sigma_{mech}$  include the use of a common-path interferometer and a reference reflector within the sample arm. In practice,  $\sigma_{\Delta\phi}$  is often appreciable due to the requirement to laterally scan across the sample, such that typical displacement sensitivities lie in the range 0.1–1 nm.

A key advantage of phase-sensitive detection over speckle tracking is its larger dynamic range. If we consider the phase difference between two A-scans acquired using an OCT system with mean wavelength of 1300 nm and minimum OCT SNR of 30 dB, the displacement dynamic range in air is  $>60$ , almost 20-fold larger than that achievable using the cross-correlation method for speckle tracking described in Sect. 32.3.1.

A major limitation is imposed by phase wrapping, one which invalidates the assumption of a linear relationship between phase difference and displacement (Eq. 32.13). Phase jumps of  $2\pi$  not only occur when the desired phase difference is close to the  $2\pi$  limit but also arise due to noise when the OCT SNR is low. In the case of dynamic loading, phase wrapping due to noise can be mitigated by faster acquisition. An alternative means of mitigation is intensity thresholding and weighting, which gives preference to the phase difference estimated from pixels with high SNR. On the other hand, robust algorithms to correctly unwrap phase may enable significant increases in the dynamic range of phase-sensitive OCE, e.g., successfully unwrapping one such event would lead to a 3 dB improvement in dynamic range. However, it must be emphasized that all phase-unwrapping algorithms break down in the presence of high noise.

Phase-sensitive detection possesses several advantages over speckle tracking, including the larger dynamic range, lower computational complexity, and higher displacement sensitivity. Also, the spatial resolution of displacement measurements is matched to that of the underlying OCT system: the displacement is not estimated in an  $X \times Z$  window, as is the case in speckle tracking.

The above discussion has not explicitly considered determining the displacement by phase measurement under dynamic mechanical loading. Liang et al. [46] developed a technique to measure displacement under dynamic loading using phase-sensitive detection. The vibration amplitude is calculated from the displacement and used to estimate the strain rate. A related technique has also been presented for measuring vibration within the ear [45]. In the next section, we consider a recently introduced improvement over these phase-sensitive methods for detecting vibration amplitude.

### 32.3.3 Doppler Spectrum

A major limitation of phase-sensitive detection is the large drop-off in accuracy with decreasing SNR (Eq. 32.14). Recently, with the goal of reducing this drop-off, a new technique has been proposed for extracting the displacement from the measured intensity under dynamic mechanical loading. Joint spectral- and time-domain optical coherence elastography (STdOCE) improves vibration amplitude measurement in dynamic OCE [47] by adapting the technique previously proposed for Doppler flow imaging [48]. STdOCE provides more accurate vibration amplitude measurements than the phase-sensitive technique in the case of low OCT SNR ( $<20$  dB), thereby extending the depth range of accurate dynamic OCE measurements.

Dynamic loading results in an amplitude spectrum of frequency tones described by Bessel functions of the first kind. In STdOCE, a Fourier transform is performed in the time domain, i.e., across multiple A-scans. If the A-scan rate is much higher than the loading rate, the result is a Doppler spectrum containing frequency tones, which can be used to extract the vibration amplitude at each depth in the sample.

STdOCE is closely related to a previously reported dynamic OCE technique based solely on time-domain (TD) OCT [19, 49]. The bandwidth of the frequency tones in TD-OCT increases with both the bandwidth of the source and the A-scan velocity, which causes them to overlap in frequency and restricts measurements to only the first few tones. This limits the accuracy and requires the use of a very slow A-scan acquisition rate ( $\sim 1$  Hz). Nonetheless, this technique was capable of being used to demonstrate the first in vivo dynamic OCE measurements [49].

In STdOCE, the increased number of tones in the Doppler spectrum provided by spectral-domain (SD) OCT allows a signal processing technique proposed in ultrasound elastography to be employed [50], in which the vibration amplitude is determined from the variance or spectral spread of frequency tones in the Doppler spectrum. Figure 32.5 shows the data acquisition and processing procedure for

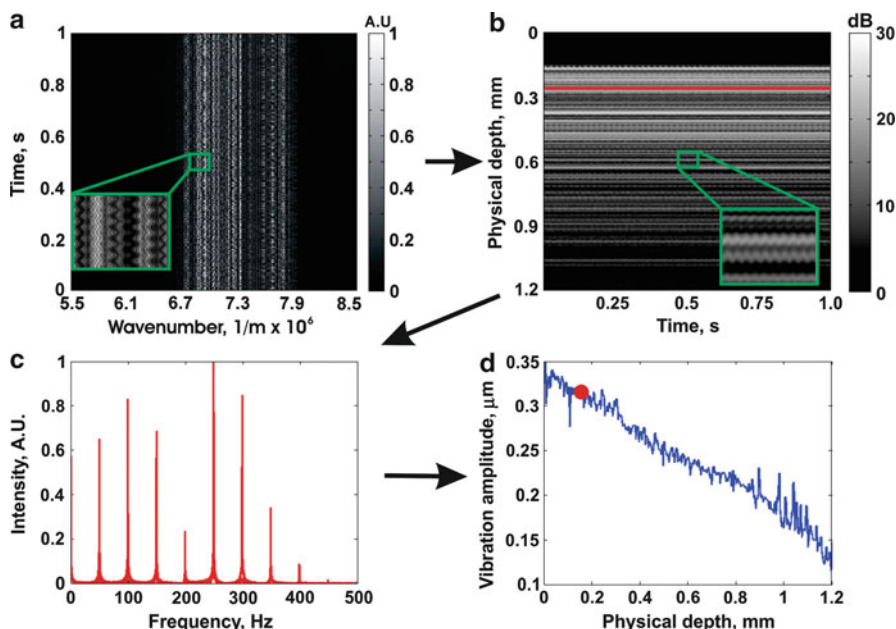


**Fig. 32.5** Data processing procedure for STdOCE: (a) 2,000 spectral interferograms; (b) A-scans obtained after Fourier transform in  $k$ -space; (c) Doppler spectrum after Fourier transform in time, performed at depth indicated by the red line in (b); and (d) vibration amplitude (peak) calculated using the spectral spread algorithm. The red dot in (d) corresponds to the vibration amplitude calculated from the Doppler spectrum in (c) (reproduced from [47])

STdOCE. In Fig. 32.5a, 2,000 successive spectral interferograms acquired from the same lateral position in a homogeneous phantom are shown. In Fig. 32.5b, the corresponding depth-resolved A-scans, after Fourier transformation in  $k$ -space, are shown. In Fig. 32.5c, the Doppler spectrum obtained after performing a second Fourier transform in the time domain at the depth indicated by the red line in Fig. 32.5b is shown, with nine overtones in evidence. Having calculated the Doppler spectrum, the spectral spread algorithm is used to calculate the vibration amplitude. The vibration amplitude calculated from the spectrum in Fig. 32.5c is indicated by the red dot in Fig. 32.5d. This procedure is repeated for each depth in the sample, allowing a vibration amplitude plot (blue line in Fig. 32.5d) to be generated.

Figure 32.6 demonstrates the superiority of STdOCE over a representative technique for phase-sensitive detection [45]. In Fig. 32.6a, a structural OCT image of a soft phantom containing a stiff inclusion is shown. The inclusion is located in the center of the image and is indicated by the labeled arrow. Below the inclusion, a shadow artifact, corresponding to a region of low OCT SNR, is also labeled. A plot of the OCT SNR, at the lateral position indicated by the vertical red arrow in Fig. 32.6a, is shown in Fig. 32.6d. Vibration amplitude images generated using STdOCE and phase-sensitive OCE are shown in Fig. 32.6b, f, respectively. In both

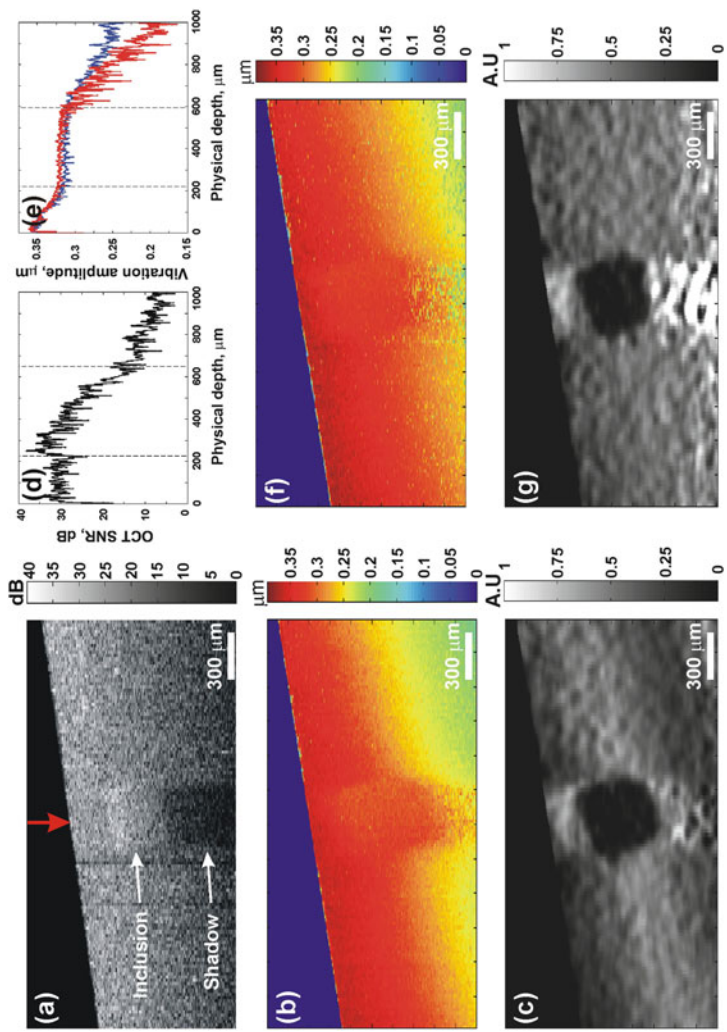


**Fig. 32.6** Soft phantom containing a stiff inclusion: (a) OCT structural image; (b) vibration amplitude image; (c) elastogram for STdOCE; (d) OCT A-scan; (e) vibration amplitude plots for STdOCE (blue) and phase-sensitive OCE (red) at the lateral position indicated by the red arrow in (a), where the dashed lines in (d) and (e) indicate the boundaries between the soft bulk and hard inclusion; (f) vibration amplitude image; and (g) elastogram for phase-sensitive OCE [47]

**Table 33.1** Comparison of different methods to measure displacement in OCE

	Minimum displacement	Maximum displacement	Axial resolution	Lateral resolution	Dimension of elasticity measured	Minimum data required
Speckle tracking	$\sim 0.1 \times$ pixel size	$\sim 0.5 \times$ OCT resolution	$5\text{--}10 \times$ OCT resolution	$5\text{--}10 \times$ OCT resolution	1D, 2D, 3D	2 A-scans
Phase-sensitive	$\sim 20$ pm	$\sim 0.5 \times$ source wavelength	OCT resolution	OCT resolution	1D	2 A-scans
Doppler spectrum	$\sim 10$ nm	$\sim 0.5 \times$ OCT axial resolution	OCT resolution	OCT resolution	1D	$>10$ A-scans

images, the stiff inclusions are denoted by the lower rate of change in vibration amplitude with depth, i.e., lower strain. Vibration amplitude plots generated using both techniques, at the lateral position indicated by the red arrow in Fig. 32.6a, are shown in Fig. 32.6e. Both plots match well until a depth of  $\sim 600$   $\mu\text{m}$ . At depths  $>600$   $\mu\text{m}$ , the decrease in vibration amplitude is higher for the phase-sensitive technique (red). This is caused by an underestimation of the vibration amplitude in the low OCT SNR region below the inclusion. In comparison, the decrease in vibration amplitude with depth measured with STdOCE below the inclusion is the same as that above the inclusion, as expected for these mechanically uniform regions. The strain elastograms corresponding to Figs. 32.6b and f are shown in Figs. 32.6c and g, respectively. The artificially high strain in the phase-sensitive elastogram (Fig. 32.6g) is clearly visible below the inclusion. As the elastogram is used as a surrogate for elasticity, this leads to errors in the interpretation of elastograms.

In this section, we described the two main techniques used to measure the displacement in OCE: the technique used in early OCE papers, speckle tracking, and the most commonly used technique in recent papers, phase-sensitive OCE. A recent improvement on phase-sensitive OCE that applies to dynamic displacement, STdOCE, based on the analysis of the Doppler spectrum, was also described. As discussed, each technique has its advantages and disadvantages, and these are summarized in the table below. It is expected that phase-sensitive techniques will continue to be prominent, as they enjoy a significantly larger dynamic range than speckle tracking and require the acquisition of much less data than STdOCE (Table 32.1).

## 32.4 OCE Techniques

In this section, we consider the wide variety of techniques that have been used to estimate elasticity from the measured displacement, as categorized by the nature and dynamics of the loading mechanism. We divide OCE techniques into five categories: compression, surface acoustic wave, acoustic radiation force, magnetomotive, and spectroscopic.

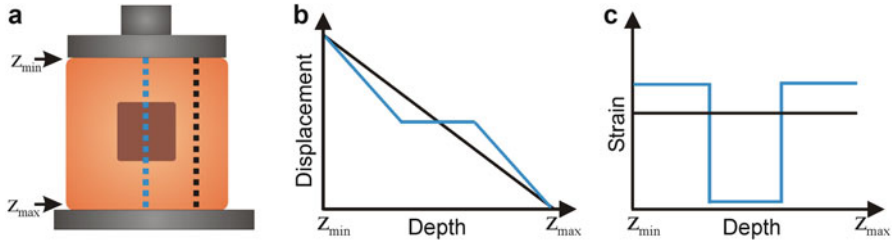


**Fig. 32.7** (a) Illustration of an external load applied to a tissue sample, (b) tissue displacement versus depth for the positions indicated by the blue and black lines in (a), and (c) corresponding strain versus depth

### 32.4.1 Compression

In compression OCE, a step load is introduced externally to a sample between acquisitions (of either A-scans or B-scans) and the strain is estimated from the change in measured displacement with depth. This technique was used by Schmitt et al. in the first demonstration of OCE [9]. Compression elastography is the most straightforward to implement and is also the most mature in ultrasound elastography [3, 5]. In compression OCE, a number of assumptions are commonly made: (1) the stress is uniformly distributed throughout the sample, allowing the strain to be used as a surrogate for elasticity; (2) the sample is linearly elastic; and (3) it compresses uniaxially. These assumptions are also made in a number of dynamic OCE techniques [19, 49, 51], with one notable exception [52]. The adequacy and appropriateness of these assumptions is discussed in detail in Sect. 33.6.

The basic principle of compression OCE is illustrated in Fig. 32.7. A soft material containing a stiff inclusion, resting on a rigid, immovable surface, is subjected to a step load by an external compression plate. The displacement versus depth introduced at the positions indicated by the black and blue lines in Fig. 32.7a is shown in Fig. 32.7b. The displacement in the homogeneous region of the sample (black line) decreases linearly to zero at  $z_{max}$ , i.e., the sample undergoes uniform compression. The displacement through the center of the sample (blue curve) shows a local deviation in the displacement in the region corresponding to the stiff inclusion. Assuming the inclusion has a Young's modulus much larger than the background material, it can be considered to displace as a bulk, i.e., the displacement at each position in the inclusion is equal.

In Fig. 32.7b, the presence of the inclusion can be readily distinguished from the displacement. However, the difference in slope would be less visible if the stiffness of the inclusion approached that of the bulk medium. Furthermore, displacement alone cannot be used to quantify stiffness, as the displacement at a given depth in the sample is also dependent on the distance from the load. To overcome these issues, the uniaxial local strain, i.e.,  $\partial u_z / \partial z$  in the strain tensor (Eq. 32.4), may be plotted. The local strain corresponding to the displacement plots in Fig. 32.7b is plotted in Fig. 32.7c. The homogeneous region (black line) undergoes constant strain versus depth, whereas the hard inclusion undergoes a locally reduced strain

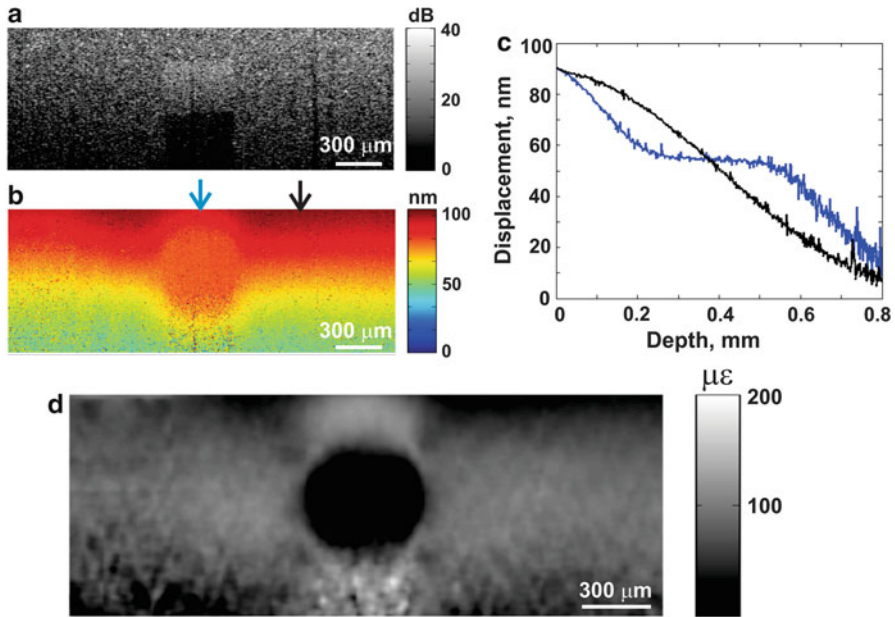


**Fig. 32.8** (a) OCT image of a soft phantom containing a stiff inclusion, (b) displacement map generated for a load similar to that shown in Fig. 32.7a, (c) displacement plots corresponding to the positions indicated by the blue and black arrows in (b), and (d) elastogram generated from the displacement map in (b)

(zero strain in the ideal case of bulk motion of the inclusion shown here). It should also be noted that because the total change in displacement from  $z_{\max}$  to  $z_{\min}$  is the same in both regions, the strain above and below the inclusion is higher than that in the homogeneous region.

Experimental phase-sensitive compression OCE results from a phantom similar to the sample illustrated in Fig. 32.7, i.e., a stiff inclusion embedded in a soft surrounding material, are presented in Fig. 32.8. In Fig. 32.8a, the OCT image is shown. The inclusion is visible in the center of this image. The displacement map calculated from the phase difference between B-scans is shown in Fig. 32.8b and the displacement plots, similar to those illustrated in Fig. 32.7b, are presented in Fig. 32.8c at the lateral positions indicated by the arrows in Fig. 32.8b. In Fig. 32.8d, the corresponding strain image is presented. Each pixel in this image corresponds to the local strain estimated at that spatial location. The local strain is presented in  $\mu\epsilon$ , signifying microstrain. As expected, the stiff inclusion has lower strain than the surrounding soft material. The strain is estimated as the change in displacement,  $\Delta u_z$ , over a depth increment,  $\Delta z$ , which, in turn, defines the strain axial resolution [53]. This estimation results in an inherent loss of spatial (axial) resolution in compression OCE. For the results shown in Fig. 32.8d,  $\Delta z$  was 75  $\mu\text{m}$ , while the axial resolution of the OCT system was  $\sim 8 \mu\text{m}$ . Although it is a qualitative measurement of elasticity (in the sense that local strain cannot be

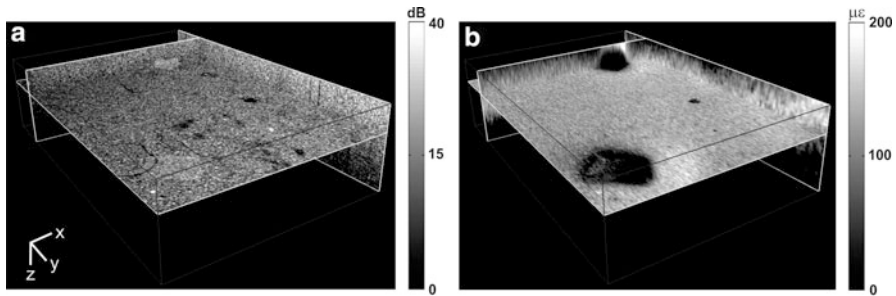


**Fig. 32.9** 3D-OCT (a, b) compression 3D-OCE images of the same soft phantom with two stiff inclusions visible, showing enhanced mechanical over scattering contrast for the chosen values of scattering strength and stiffness. Scale bars represent 200  $\mu\text{m}$

used to determine modulus because the local stress is not known), we define the strain image as an elastogram.

The two major factors in determining the strain measurement accuracy are the displacement measured from the OCT data and the method used to calculate strain from the measured displacement. The techniques used to measure displacement were discussed in detail in Sect. 32.3. Four estimation methods have been used to determine strain in compression OCE: finite difference, ordinary least squares, weighted least squares, and Gaussian smoothed weighted least squares (GS-WLS) [53]. In order to compare these methods, strain imaging parameters have been defined. The strain sensitivity,  $S_\epsilon$ , is defined as the standard deviation of the strain estimate,  $\sigma_\epsilon$ , and the strain SNR,  $SNR_\epsilon$ , is defined as the ratio of the mean to the standard deviation of the strain estimate,  $\mu_\epsilon/\sigma_\epsilon$ . The GS-WLS method has been shown to provide an improvement in both sensitivity and SNR of 3 dB compared with weighted least squares, 7 dB compared with ordinary least squares, and 12 dB compared with finite difference. For all methods, strain spatial resolutions  $<40 \mu\text{m}$  did not provide accurate strain estimation [53].

3D visualizations of an OCT image and the corresponding elastogram, generated using GS-WLS strain estimation, are presented in Fig. 32.9. The sample is a soft silicone phantom containing two stiff inclusions. The elastogram axial resolution is 75  $\mu\text{m}$ , and the lateral resolution is 10  $\mu\text{m}$ . The inclusions are more readily visible in the elastogram than in the OCT image, demonstrating the potential of compression OCE to provide additional contrast in comparison with OCT. The subject of strain contrast in compression OCE will be discussed in greater detail in Sect. 32.6.

### 32.4.2 Surface Acoustic Wave

In recent years, a number of OCE techniques based on the measurement of the velocity of waves propagating along the sample surface have emerged [14, 15, 25, 54–57]. The shear modulus can be extracted from this velocity measurement using

inverse methods. Proposed techniques have used phase-sensitive detection in SD-OCT [54, 55], swept-source OCT [25, 57], and digital holography [14, 15]. In this subsection, we focus on the technique employing holographic detection.

Digital holographic imaging (DHI) is in many ways similar to OCT, as it is an interferometric technique that provides both the amplitude and phase of light scattered from an object. As such, it is similarly sensitive to tissue displacements, on the order of a fraction of the light wavelength. The primary difference is that DHI typically uses a long-coherence length light source that does not provide depth-resolved imaging. At the same time, DHI more naturally provides tissue surface displacement imaging over wide areas, ranging from imaging of vibrations on an eardrum [58], to induced vibrations over the whole human body [59]. Because DHI provides such comprehensive surface displacement data, it is helpful to look toward other areas of science where surface data have been employed for elasticity measurements. In fact, nondestructive testing has been widely employed to analyze the integrity of structural materials, where inversion of vibration data to produce a quantitative elastogram is treated as a boundary value problem [60, 61]. On a much larger scale, seismology is concerned with the analysis of the earth's surface movements (e.g., from earthquakes), which has been used to produce maps of the stiffness within the interior of the earth [62].

In seismology, the depth-dependent stiffness of, e.g., layers of rock, is often found by analysis of Rayleigh waves (also known as surface acoustic waves or SAWs) [63]. The ability to depth-resolve elasticity using SAWs is due to two key features of the waves: (1) SAWs propagate laterally with a penetration depth proportional to their wavelength and, thus, are only “sensitive” to materials within this characteristic depth, and (2) the wave velocity depends upon the material's Young's modulus  $E$  within this sensitive region (which we will define as our sensitivity kernel) according to  $c_R \approx \frac{0.87+1.12\nu}{1+\nu} \sqrt{\frac{E}{2\rho(1+\nu)}}$ , where  $\nu$  is Poisson's ratio and  $\rho$  is mass density (both of which vary only slightly in tissue). As illustrated in Fig. 32.10, we can therefore measure SAW velocity versus frequency and use this to infer the depth-dependent elasticity. A stiff surface layer with an underlying soft layer will appear as a positive dispersion in the SAWs (i.e., wave speed increasing with frequency) because higher frequency waves “feel” only the stiffer surface material, resulting in higher velocity. Conversely, a soft surface layer with stiff underlying layer is negatively dispersed.

By using an appropriate model for the sensitivity kernel of the SAWs, one can construct a linear system relating a measurement of the SAW velocity dispersion,  $c_R(f)$ , to the 1D depth-dependent Young's modulus of the sample,  $E(z)$ . This inverse method was first demonstrated in soft materials using a single-point optical vibrometer scanned away from a point source actuator [64, 65]. It was subsequently translated to DHI, where depth-resolved elasticity was measured in 2-layer phantoms up to 55 mm deep (Fig. 32.10 panels e, f) [15]. The advantage of using DHI to perform SAW elastography is the capability for real-time imaging of SAWs across the entire tissue surface, extending the 1D measurement of  $E$  into three dimensions. Importantly, this could have applications in performing whole-breast elastography,

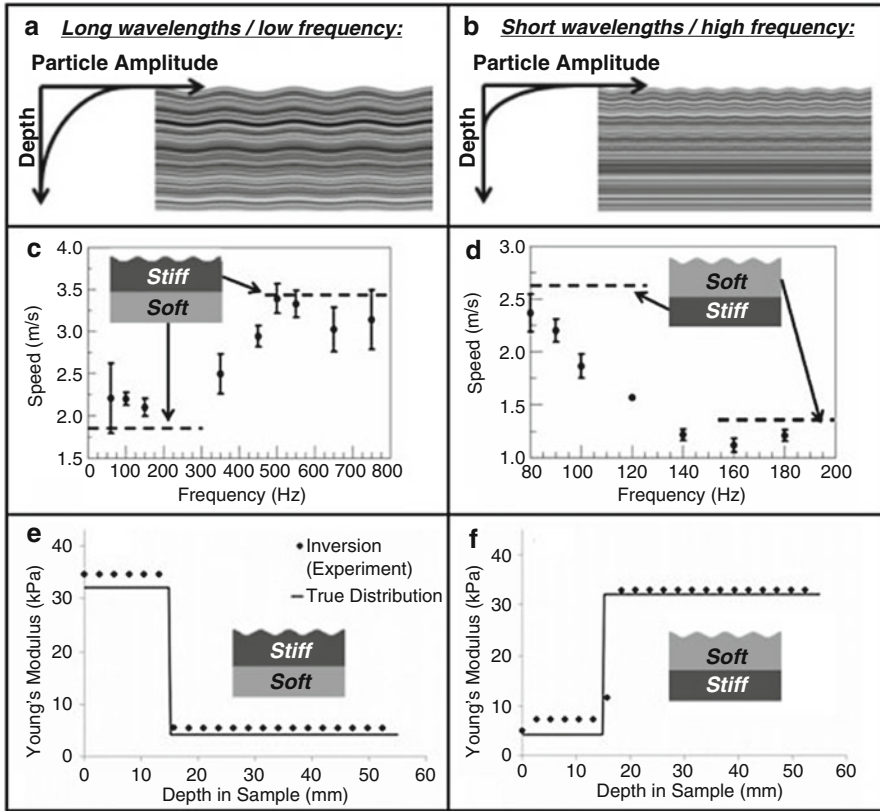


**Fig. 32.10** Relationship between velocity dispersion of SAWs and depth-dependent stiffness. (a, b) Schematic illustration of SAWs versus depth showing how frequency affects the depth of penetration. (c, d) SAW velocity dispersion curves obtained using DHI in 2-layer tissue phantoms (data reprinted from [14]). (e, f) Reconstructed elastic depth profile in 2-layer phantoms is consistent with the actual phantom stiffness (Data reprinted from [15])

as a quantitative method to replace manual palpation currently used in breast cancer screening. In materials of similar elasticity as the human breast, SAW frequency sweeps from 20 to 600 Hz would be expected to provide elastograms over depths from nominally 5–50 mm. Currently, it has been qualitatively shown that DHI can detect perturbations in SAWs propagating over a 5 mm tumor-like inclusion embedded 9 mm deep in a breast tissue phantom [15] and that SAWs on real tissues appear well behaved when visualized with DHI (Fig. 32.11).

The visualization of SAWs using DHI deserves some attention here. There are several standard techniques employed in DHI for dynamic displacement measurement, which typically include off-axis holography and either Fourier transformation or spatial phase-shifting of the resulting fringe pattern [66, 67]. Interestingly, SAW elastography only requires measurement of the SAW phase velocity under a condition of a priori knowledge of the SAW frequency. Using this advantage, a method was recently

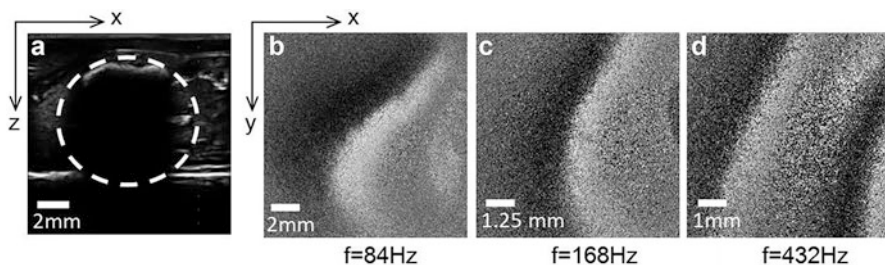


**Fig. 32.11** Imaging SAWs in chicken thigh. (a) B-mode ultrasound showing the depth position of the thigh bone (*dashed circle*). (b–d) Corresponding DHI phase maps of SAWs propagating on the surface as a function of frequency. While low-frequency SAWs are strongly perturbed by the presence of the bone, well-behaved SAWs at high frequencies suggest that the softer tissue above the bone is relatively elastically homogeneous (Reprinted from [15])

developed to extract SAW phase (modulo  $\pi$ ) using an on-axis DHI system without any phase modulation [14]. This method circumvents the limitation to the maximum spatial frequency of fringes imposed by off-axis holography, with the trade-off that one cannot readily extract the amplitude of the SAWs (only the phase). Example SAW phase maps obtained from chicken tissue are displayed in Fig. 32.11, revealing apparent wave “crests” corresponding to where the SAW phase wraps from  $\pi$  back to zero, which is a very intuitive way of visualizing the SAW wave fronts.

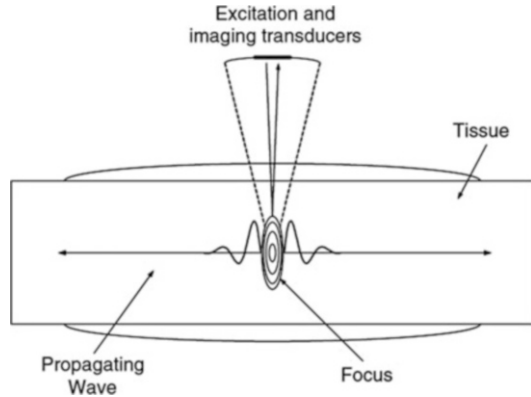
In summary, DHI-based elastography is a promising method for quantitative elastography that exploits the depth-penetrating property of SAWs to provide elastography several centimeters into tissues. Importantly, it is not limited by the shallow depth penetration of light but trades off overall spatial resolution. While standard elastography requires 3+1D (spatial+temporal) data collection, SAW-based elastography requires only 2+1D (spatial+frequency) data collection with the use of an appropriate model for SAWs to solve the boundary value problem. Future emphasis in this area will be on extending the current quantitative 1D elastography method to 3D.

### 32.4.3 Acoustic Radiation Force

In acoustic radiation force impulse (ARFI) imaging, a focused ultrasound pulse creates a localized mechanical load within a sample and the resulting deformation is measured using imaging techniques. Its initial development was based on ultrasound detection [68], with continuing clinical and commercial interest [69, 70]. More recently, OCT-based ARFI has been proposed, allowing smaller displacements to be measured with improved spatial resolution [23, 26, 71, 72].

Consider an acoustic wave, propagating in tissue generated using an ultrasound transducer. A unidirectional force is applied to absorbing or reflecting targets in the propagation path of the acoustic wave. This force results from a transfer of momentum from the acoustic wave to the tissue. Under the assumption of plane

**Fig. 32.12** Illustration of shear wave propagation caused by a focused ultrasound pulse (Reproduced from [2])



wave propagation, the acoustic body force (i.e., force per unit volume) applied to tissue at a given location due to local absorption is given by  $F = \frac{2\alpha I}{c}$ , where  $F$  has units of  $\text{kg}/(\text{s}^2\text{cm}^2)$ ,  $c$  is the speed of sound (m/s) in the tissue,  $\alpha$  is the tissue absorption coefficient ( $\text{m}^{-1}$ ), and  $I$  is the average intensity of the acoustic beam ( $\text{W}/\text{cm}^2$ ) at the given location.

On-off modulation of the acoustic wave results in a corresponding on-off modulation of the local force and, hence, displacement, which can be measured directly or through the generation of an accompanying shear wave propagating in the direction perpendicular to the direction of the focused ultrasound beam, as illustrated in Fig. 32.12. The goal in ARFI imaging has primarily been to measure the sub-surface shear wave speed,  $c_s$ , which is directly related to the sample's shear modulus,  $\mu$ , by  $c_s = \sqrt{\mu/\rho}$ , where  $\rho$  is the density of the tissue. Both speckle tracking [71] and phase-sensitive detection [23, 26] have been used to measure the shear wave speed in ARF-OCE. Axial displacement has also been measured in an ARF-OCE technique [72].

A related ARFI technique known as transient optoelastography has also been proposed [12, 73]. This technique is based on ultrasound-modulated optical tomography (UMOT) [13]. Detection of variations in laser speckle patterns recorded on the surface of a sample due to acoustic stimulation at depths up to several centimeters is possible, providing information from much greater depths than possible using OCE. However, the spatial resolution is determined by that of the ultrasound beam and is, therefore, much lower than that of OCE.

In all ARFI techniques, it should be considered that the high-intensity acoustic pulses used can be potentially harmful and above the safe limits set by, e.g., the U.S. Food and Drug Administration (FDA) [68]. However, this may prove not to be a major concern in ARF-OCE, as much smaller tissue displacements are required than when using ultrasound detection. Another noteworthy issue is the use of water or gel to couple the transducer and sample required to achieve acoustic impedance matching. Furthermore, same-side optical imaging and acoustic loading requires use of an annular or off-axis acoustic transducer.

### 32.4.4 Magnetomotive

Magnetomotive OCE (MM-OCE) utilizes an external magnetic field to induce magnetomotion within a sample of interest and OCT to detect displacements within the sample on the order of tens to hundreds of nanometers. Magnetomotion can be produced via internal excitation through the use of magnetic nanoparticles (MNPs) distributed within the sample [74–76], through a magnetic implant embedded in a sample [77], or via external excitation, e.g., through the use of a metallic slab transducer placed in contact with the sample [78]. MM-OCE can perform optical rheology of viscoelastic materials by measuring the dynamic response of a sample, either to a step excitation [74] or to a frequency sweep [75, 78]. The natural resonant frequencies of the sample can be connected to elastic and viscous moduli through an appropriate mechanical model.

The use of step excitation for optical rheology of tissue phantoms is shown in Fig. 32.13. These measurements were carried out in silicone phantoms doped with titanium dioxide particles to provide optical scattering and iron oxide MNPs to provide internal magnetomotive forces. Motion-mode (M-mode) measurements show an under-damped response to the (broadband) step excitation, where the dominant relaxation frequency is the natural resonance of the sample. The Young's modulus of the samples was varied over a range from 0.4 to 140 kPa, as calibrated using a commercial indentation instrument. The resonant frequency of the sample showed a linear dependence versus the square root of the Young's modulus, which is consistent with the behavior of a Voigt model, as previously adopted to model the mechanical response of bulk tissue [52].

Magnetomotive resonant acoustic spectroscopy (MRAS) is another magnetomotive technique to measure tissue elasticity [75]. MRAS utilizes a frequency sweep to measure the natural resonant frequencies of tissue-mimicking phantoms and biological samples. This approach provides improved signal-to-noise ratio compared to the step excitation, due to the increased measurement time of the sweep. Experiments in tissue-mimicking phantoms confirmed that the longitudinal vibration modes (natural resonant frequencies of the sample) depended on both sample viscoelastic properties as well as the geometrical dimensions (cylinder aspect ratio). For known sample geometry, Young's modulus and the viscous damping coefficient of the samples were determined by fitting the data to a viscoelastic mechanical model. In this model, Young's modulus was proportional to the square of the resonant frequency, while the viscous damping coefficient was proportional to the Lorentzian-shaped linewidth (related to the quality factor  $Q$ ) of the resonant peak.

With biological tissue, where the geometry of the sample is not well controlled, MRAS has shown the ability to track relative changes in Young's modulus of the sample. Figure 32.14a shows measurements of the complex mechanical spectrum of rat liver undergoing formalin fixation. The increase in the resonant frequency with time can be seen in both the amplitude and phase of the mechanical response. Over a period of 147 min, the resonant frequency of the tissue undergoing fixation increased by a factor of 2, which suggests an increase in Young's modulus by a factor of 4.

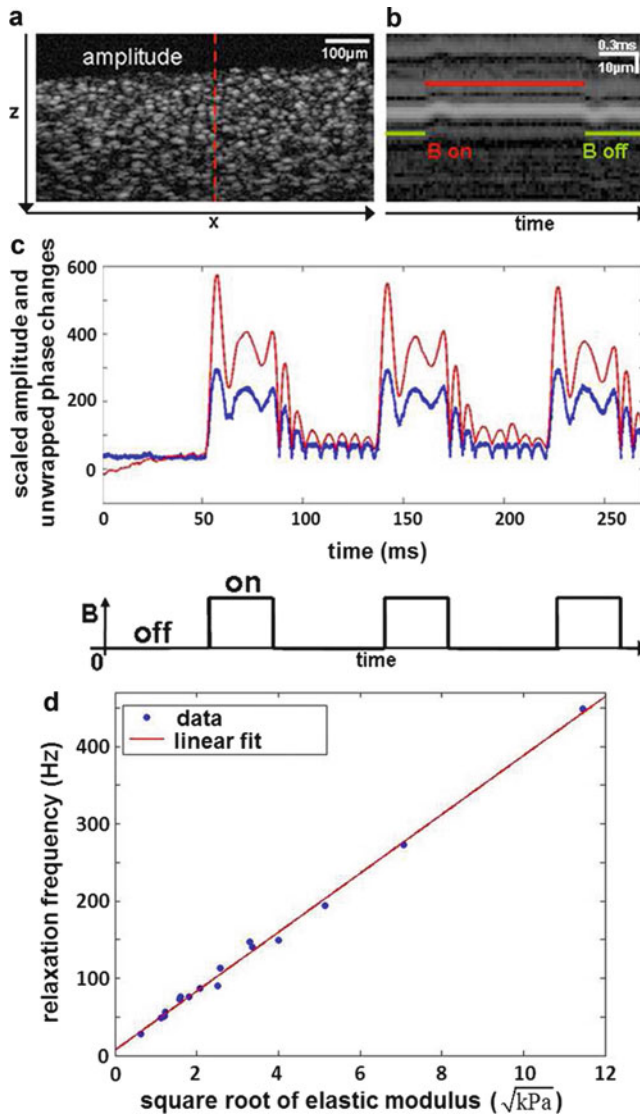


**Fig. 32.13** Optical rheology of tissue phantoms based on a step magnetic excitation. (a) Cross-sectional OCT image. (b) M-mode image at the transverse position denoted by the *dashed red line* in (a). (c) Average scatterer response showing the amplitude (*blue*) and phase (*red*) characteristics of the magnetomotion from the excitation profile shown directly below (c). (d) The natural resonance frequency of phantoms of varying stiffness (adapted from [74])

MRAS was utilized in a subsequent study to evaluate the dependence of the resonant frequency of fibrin clots vs. fibrinogen concentration [78]. The viscoelastic properties of fibrin networks are important in bleeding and clotting disorders. Clots were formed with controlled geometry in custom-printed rectangular wells, and in

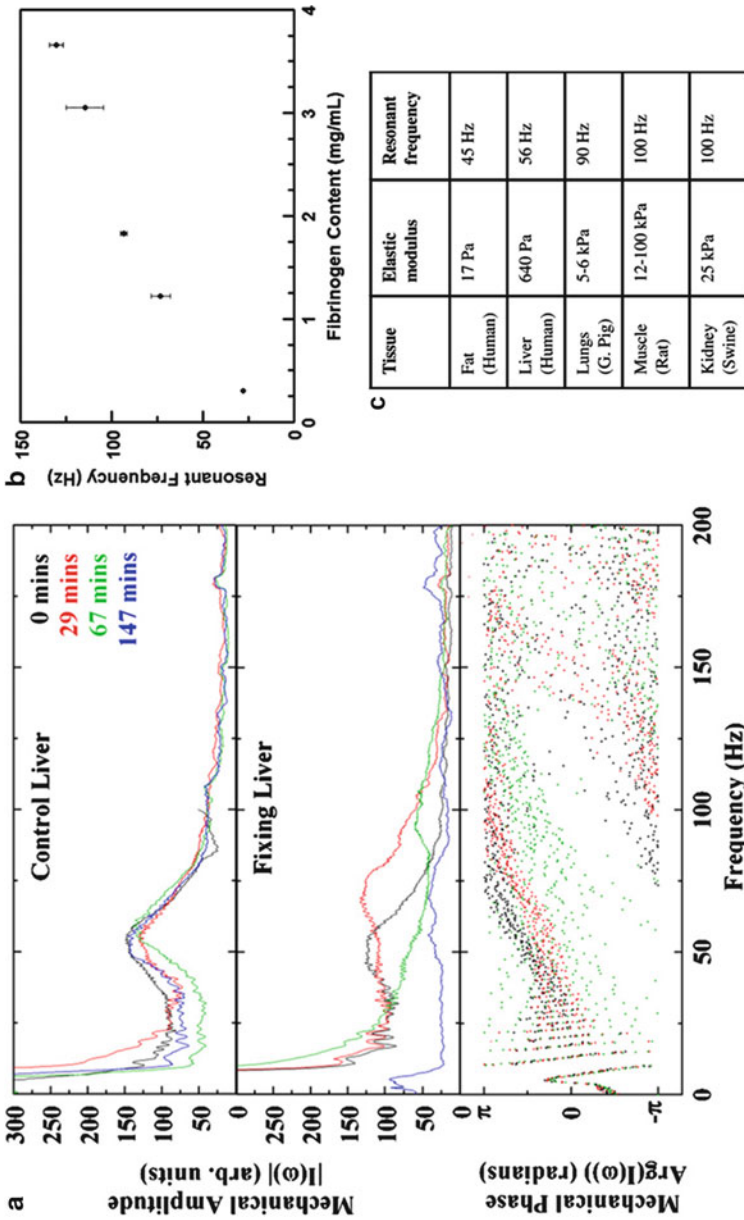


**Fig. 32.14** MRAS of biological samples. (a) Longitudinal tracking of rat liver tissue undergoing formalin fixation ex vivo (from [75]), (b) resonant frequency of fibrin clots prepared in custom-printed rectangular wells (From [78]), and (c) table of natural resonant frequencies for different tissues (From [79]). Magnetomotion was produced via internal iron-oxide MNPs in (a) and (c), but with an external microtransducer in (b)

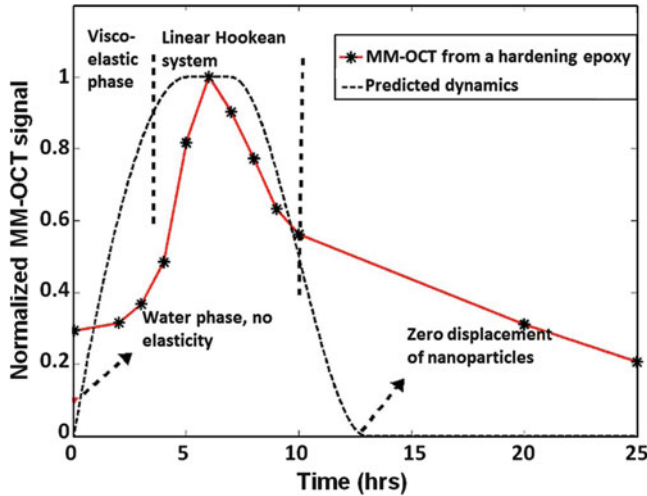


**Fig. 32.15** Magnetomotive response of an epoxy sample undergoing transition from a viscous liquid state to a rigid solid (Adapted from [79])

this study an external microtransducer was used in order to avoid embedding the clots with MNP nanotransducers. Figure 32.14b presents results from M-mode measurements, showing that the resonant frequency increases monotonically with fibrinogen concentration. The Young's modulus is proportional to the square of the resonant frequency. Figure 32.14c presents measurements of the natural vibration frequencies for different types of tissues [79].

The magnetomotion facilitated by MNPs has been investigated in a wide range of viscoelastic conditions [79], experimentally simulated through the hardening process of epoxy from a viscous liquid to its final hardened state (see Fig. 32.15). The epoxy had a characteristic setting time of 12 h at a temperature of 90 °C. The low initial MM-OCT signal shows that initially the MNPs are not bound within the viscous fluid and so experience virtually no elastic restoring forces. Since the direction of the magnetic gradient force is the same regardless of polarity of the magnetic field [75], the oscillating magnetic field simply results in unidirectional displacements in addition to the Brownian motion of the particles in the liquid. Since the signal processing detects only sinusoidal motion, the liquid phase regime does not generate an appreciable MM-OCT signal. As the epoxy sets, it enters the regime of a linear Hookean system, where the MNPs that are now bound to the matrix experience elastic restoring forces. Finally, as the epoxy hardens the MNPs become tightly bound to the medium (which now has a significantly increased elastic constant), and the magnetomotion tends to zero. Ongoing work with a dual coil setup will enable bipolar forces on the magnetic particles, to extend the regime of applicability of MM-OCE to highly viscous samples [80].

Further work on MM-OCE will investigate the contributions of tissue geometry to the complex mechanical spectra and the extraction of quantitative mechanical properties. Finite element modeling, discussed in detail in Sect. 32.6, can simulate

deformation due to magnetomotive forces in irregularly shaped samples and help disentangle the impact of biomechanical heterogeneity on the bulk natural vibration modes of the sample. Extending these M-mode MM-OCE measurements to perform B-mode (or volumetric) imaging has the potential to provide spatially localized information on the mechanical properties of heterogeneous samples.

### 32.4.5 Spectroscopic

Mechanical spectroscopic imaging of tissue was first reported in landmark papers on ultrasound-stimulated vibro-acoustography [81, 82]. Vibro-acoustography utilizes the radiation force of focused ultrasound (see Sect. 32.4.3) within tissue to excite sinusoidal motion in the kHz regime and a sensitive hydrophone to detect the amplitude and phase of the resulting acoustic emission. Instead of pulsed ultrasound considered in Sect. 32.4.3, local excitation in the kHz regime was achieved through the use of two confocal ultrasonic transducers (each operating at  $\sim 3$  MHz) to generate at their difference frequency a kHz oscillation of the ultrasonic energy density at the overlap of the foci. These overlapped foci were raster scanned within the sample to record an image of the object motion. Mechanical spectroscopy was performed by tuning the difference (beat) frequency between the transducers. Vibro-acoustic spectrography of human iliac arteries *ex vivo* demonstrated clear differences between stiffer calcified regions and nearby normal regions of the artery, at an excitation frequency of 6 kHz. These differences were observed in both the (mechanical) amplitude and phase images [81].

Motivated by the success of ultrasound vibro-acoustography [83–86], mechanical spectroscopic imaging has also been developed for OCE [87]. Utilizing a spectral-domain OCT platform for phase-sensitive B-mode imaging during external mechanical excitation [32, 46], 2D B-mode images were recorded over a wide range of excitation frequencies (20–1,000 Hz). Signal processing steps were developed to extract the (spatially localized) complex mechanical displacement. Figure 32.16 shows spectroscopic OCE in rat mammary tissue consisting of tumor adjacent to adipose. Peaks in the mechanical spectra at 83 and 385 Hz were attributed to adipose and tumor regions of the tissue, respectively. Contrast between mechanically distinct regions of the tissue can be seen in both the amplitude and mechanical phase response images corresponding to 83 Hz excitation. In particular, the mechanical phase image highlighted an oval region of the sample, with a mechanical phase shift of  $+\pi$  that is characteristic behavior above resonance. The distinction of this region from its surroundings was seen over a wide frequency range (25–83 Hz, and at 125 and 167 Hz), suggesting a relatively low resonant frequency. Appearing as oval-shaped structures in the histology image, this feature was attributed as a fluid-dense follicle or vacuole.

Spectroscopic OCE is at an early stage of development and several areas require further investigation. As discussed in Sect. 32.4.4, the impact of tissue geometry,

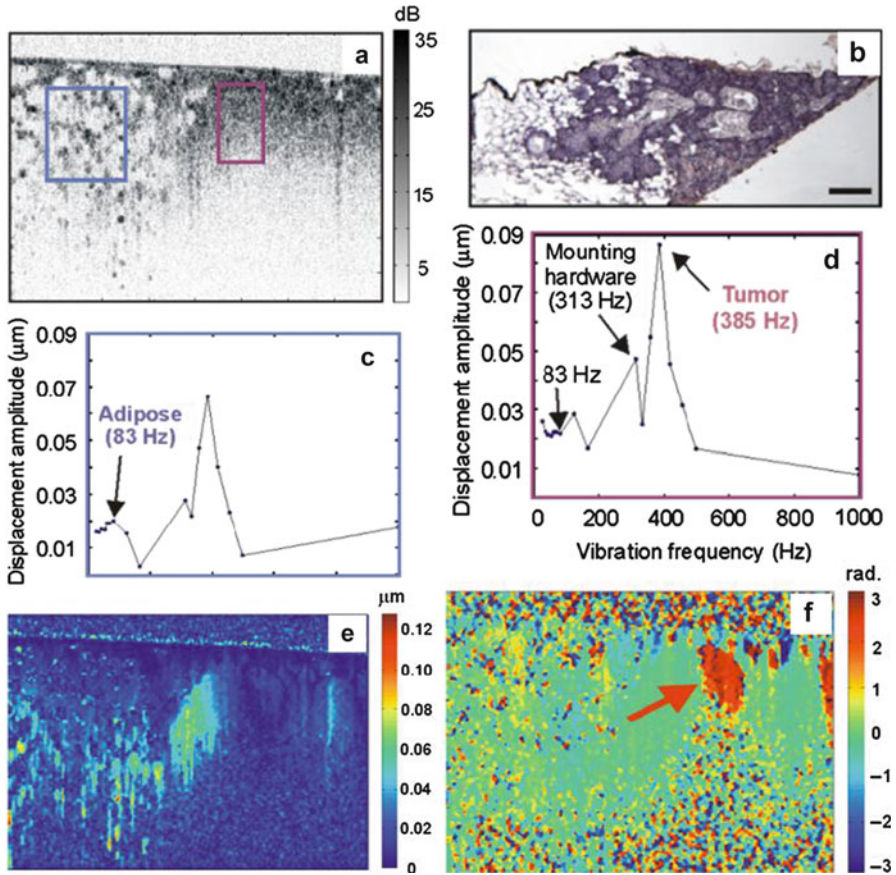


**Fig. 32.16** Spectroscopic OCE of rat mammary tumor adjacent to adipose tissue. (a) B-mode OCT image, (b) corresponding nearby histology, (c) mechanical amplitude spectrum for adipose (spatial average over blue box in (a)), (d) mechanical amplitude spectrum for tumor (spatial average over magenta box in (a)), (e) displacement amplitude image at excitation frequency of 83 Hz, and (f) displacement phase image at excitation frequency of 83 Hz (Adapted from [87])

heterogeneity, and the natural vibration modes of the mechanical mounting hardware on the complex mechanical response measured in the sample needs to be determined. Further work on theoretical modeling and simulation (see Sect. 32.6) could provide a method to invert the complex displacement maps in order to extract the elastic and viscous properties of the sample. These simulations could also investigate the role of mechanical coupling on the spatial resolution of the inversion process. ARF-OCE (see Sect. 32.4.3) is a promising approach to address potential resolution limitations with external (bulk) mechanical excitation [23]. Further work is required to adapt ARF-OCE for B-mode or volumetric spectroscopic imaging. Finally, it would be interesting to extend the excitation frequency range into the kHz regime (as in ultrasound-stimulated vibro-acoustography). Ultimately, the

success of spectroscopic OCE will depend on characterizing the appropriate frequency ranges (or specific excitation frequencies) that maximize contrast between regions of tissue with distinct biomechanical properties.

## 32.5 Implementation

Translation of OCE techniques to clinical use requires further development of practical probes that enable simultaneous loading and imaging of tissue. This section reviews initial efforts to implement OCE *in vivo*, using probes suitable for superficial tissues such as skin and catheter-based and needle-based probes suitable for use within the body.

### 32.5.1 Imaging Superficial Tissues

Most initial OCE studies performed imaging and loading of small samples from opposite sides [40, 49, 52]. While this configuration may be sufficient for imaging small *ex vivo* tissue samples or phantoms, imaging and loading from the same side are essential for *in vivo* imaging. In the first OCE paper [9], loading and imaging were performed from the same side using an annular piezoelectric actuator, but an A-scan rate of 11 Hz and decorrelation of speckle due to sample movement limited the *in vivo* capabilities of this setup. A same-side OCE setup was later proposed using a similar design [19], as shown in Fig. 32.17. An annular piezoelectric transducer is fixed to an imaging window and coupled directly to the sample, enabling simultaneous, concentric actuation and imaging of the tissue. This ring

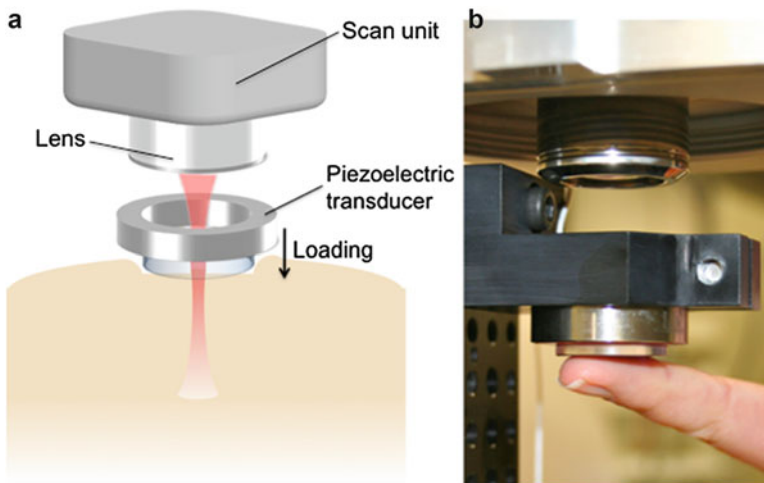


**Fig. 32.17** Ring actuator design for *in vivo* OCE of superficial tissues. (a) Probe schematic and (b) photograph of implementation for skin imaging

actuator design can be used to apply pico- to microscale displacements to tissue over a wide range of frequencies and has been used in compression and spectroscopic OCE studies [51, 87], including the first in vivo 3D OCE measurements, which used human skin as the target tissue [51].

To perform ARF-OCE or SAW-OCE requires either an impulse load or vibrational load applied to the tissue. Implementation of these dynamic loading techniques requires careful synchronization of the actuation and imaging, but they have the practical advantage that the tissue loading may be performed adjacent to the imaging, eliminating the need to combine actuation and imaging capabilities into a single device. SAW-OCE on skin in vivo has been achieved using a mechanical shaker coupled directly to the tissue [54]. The mechanical shaker employed a piezoelectric element to introduce an impulse load to the tissue, and the resulting surface waves were measured by the adjacent OCT probe. For applications where direct contact of the probe with tissue is not desirable, such as imaging of the cornea, a noncontact implementation of SAW-OCE has also been proposed using a remote laser pulse to generate surface waves [88].

Other loading techniques for superficial tissues have included an air puff system for measuring the elastic response of the cornea [89, 90] as well as an annular suction device which applies a suction force concentric with the OCT imaging to measure elasticity of skin in tension [32].

### 32.5.2 Catheter-Based OCE

Implementation of OCE using miniaturized, fiber-based probes for endoscopic and intravascular imaging presents new challenges for developing loading schemes that can be deployed in such confined spaces. One natural approach to overcoming this issue is to use physiological deformation of the tissue as the “loading” mechanism. This is especially suitable for tissues that undergo regular changes in luminal pressure, such as airways and blood vessels. This concept has been used for measurement of the elastic properties of the airway wall using anatomical OCT (*a*OCT), a long-range OCT technique for profiling of hollow organs [91]. Here, changes in airway dimensions versus pressure were measured in patients with and without obstructive lung diseases to investigate the correspondence of airway wall compliance with pathology.

Luminal pressure changes have also been proposed as a loading technique for performing intravascular OCE [92, 93]. Although physiological deformation of tissue is convenient to measure, quantitative measurement of mechanical properties requires controlled loading of the tissue. An OCT imaging catheter that achieves this has been proposed for applying acoustic radiation force at localized points deep in the body [94]. A catheter design incorporating a piezoelectric ultrasound transducer into the distal probe head has the advantage that direct contact with the tissue is not required, as the acoustic radiation force may be focused to induce a tissue “push” at a desired distance from the probe. Such a probe design, shown in Fig. 32.18, has been realized for combined OCT and ultrasound structural imaging

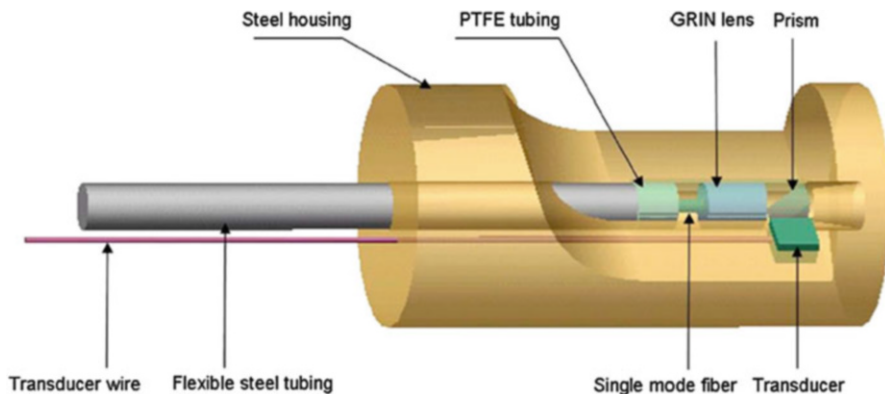


**Fig. 32.18** Schematic of combined ultrasound and OCT probe that may be suitable for performing catheter-based ARF-OCE. *PTFE* polytetrafluoroethylene, *GRIN* graded-index (Adapted from [94])

of arteries [94], but not yet been used to perform elastographic measurements. Another proposed technique for catheter-based OCE incorporates a small palpation device in the distal end of the probe, which may consist of a controlled liquid jet or mechanical indenter for compressing adjacent tissues [95]. Despite the several proposed embodiments of catheter-based OCE, results acquired using such a probe have yet to be reported.

### 32.5.3 Needle-Based OCE

The recent development of three-dimensional OCT needle probes has allowed imaging deep within solid tissues, extending potential OCT applications to include, e.g., biopsy and surgical guidance and monitoring of interstitial procedures [96, 97]. When needles are inserted into soft tissue, the needle exerts a force on the tissue ahead of the tip, as well as a shear force on the surrounding tissue due to friction. Measurement of this needle-induced deformation has been used to perform the first needle-based OCE measurements [98]. These measurements used a forward-facing probe design and phase-sensitive displacement measurement to capture 1D deformation ahead of the needle during insertion. The deformation caused by a flat end-faced needle, such as the one employed in these studies, can be approximated as compression of a column of tissue ahead of the needle [99]. Therefore, changes in the displacement with depth, i.e., the strain, indicate changes in mechanical properties.

Results from needle insertion into excised pig airway wall, consisting of layers of varying stiffness, are shown in Fig. 32.19. The displacement plot shows three distinct slopes, indicating the locations of tissue boundaries, as well as providing a measure of their relative stiffness. The displacement curve is in agreement with the corresponding histology acquired along the path of needle insertion, which shows layers of mucosa, submucosa, and smooth muscle.

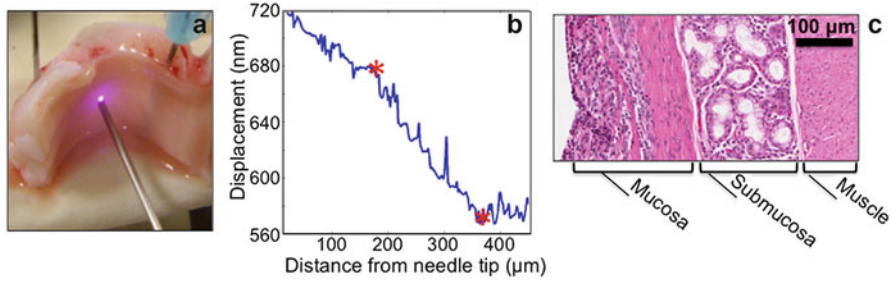


**Fig. 32.19** Needle OCE of excised pig airway wall. (a) Photograph of OCE needle probe insertion into sample; (b) measured tissue displacement ahead of the *needle tip* shows changes in slope at the positions of the *red stars*, indicating different tissue types; and (c) corresponding histology validates the presence of three tissue types (Reproduced from [98])

## 32.6 Fidelity of OCE: Comparison to Models of Tissue Deformation

In this section, we discuss artifacts that can arise in OCE and limit the accuracy with which elastograms represent the underlying elastic properties of tissue. We present initial efforts to use modeling of tissue deformation to investigate the impact of parameters such as tissue geometry and boundary conditions on the resulting contrast in elastograms. We also review initial efforts in OCE to produce more reliable, quantitative elastograms by approaching elasticity reconstruction as an inverse problem.

### 32.6.1 Limitations on the Mechanical Fidelity of Elastograms

In OCE, constructing a map of elasticity from measured displacements requires some assumptions to be made about the tissue, such that its observed behavior and mechanical properties may be linked through a mathematical model. The most common of these assumptions, which underlie image formation in compression, ARF, and SAW techniques described in Sect. 32.4, are (1) tissue is linear elastic, which allows stress and strain to be related linearly through elastic constants, and (2) tissue is isotropic (properties are direction independent), which reduces the fourth-order elasticity tensor to two elastic constants for describing the mechanical behavior of tissue (as described in Sect. 32.2.3). Magnetomotive and spectroscopic techniques (Sects. 32.4.4 and 32.4.5) have employed a more advanced model of tissue behavior, accounting for viscoelastic properties, but image formation and quantitative measurements in these techniques rely on assumptions about the tissue geometry and mechanical coupling of tissue regions.

Use of such assumptions simplifies the characterization of tissue, facilitates the development of OCE methods, and may in some cases prove sufficient for producing clinically useful images. However, tissue behavior in general is much more complex, exhibiting varying degrees of nonlinearity, viscoelasticity, poroelasticity,

anisotropy, and geometric complexity. When simple assumptions break down in the presence of such complexities, the resulting elastograms contain mechanical artifacts, limiting their fidelity to the underlying tissue properties and, ultimately, their potential clinical utility.

For OCE to advance toward clinical implementation, it is necessary to test the validity of assumptions employed in the various techniques, understand where they break down, and quantify the impact of artifacts on image contrast and reliability. Such quantitative assessment requires comparison of the measured tissue deformation in OCE to that predicted by mechanical models. Discrepancies between the two will highlight sources of mechanical artifacts and allow their effects on image contrast to be assessed. In addition to serving as an investigative tool, modeling of tissue deformation may also be used as part of an iterative elasticity reconstruction process to produce quantitative elastograms.

Accurate modeling of tissue deformation involves solving for complex geometries and heterogeneous elasticity fields, and therefore, numerical methods are preferred over analytical methods for accurate representation of tissue deformation. The predominant numerical method for modeling tissue deformation is the finite element method (FEM). In FEM, the tissue geometry is divided into a mesh of individual elements, and the governing equations of motion are solved for each element. FEM has been used in OCE to validate new methods for estimating velocity and strain [30], to validate new loading techniques for generating elastographic contrast [77, 100], and to estimate stress and strain fields in artery walls under luminal pressure [92], but has not yet been used to evaluate the limitations of mechanical artifacts on image contrast. Such investigations have been performed extensively in ultrasound elastography [101–104]. However, the impact of mechanical artifacts on image contrast in OCE will differ from those in ultrasound elastography due to different limits on measurable displacement and an increased sensitivity to boundary conditions, as images are generally limited to the first few millimeters of tissue. In the next section, we report on early efforts in using FEM to investigate sources of mechanical artifacts and evaluate their effects on image contrast for the particular case of compression elastography.

### 32.6.2 Modeling of Compression OCE

In compression elastography, strain is measured and used to represent elasticity. Interpreting strain elastograms as one-to-one representations of modulus assumes a uniform stress distribution within the sample. This assumption is invalid for samples with heterogeneous mechanical properties or when stress concentrations arise at tissue boundaries. Stress distribution beyond the sample surface cannot be measured directly, but FEM allows us to simulate the stress distribution for a given sample and investigate sources of its nonuniformity. In the case study described here, FEM is employed to simulate sample deformation in compression OCE of tissue-mimicking phantoms. The effect of feature geometry and boundary

conditions on mechanical artifacts and the resulting image contrast are investigated in both FEM and experiments.

Careful fabrication of phantoms with known geometry and mechanical properties was essential for input to the model and fair comparison of the simulated and measured sample deformation. Silicone was used, as its optical and mechanical properties can be controlled over a wide range, and it can be readily molded into complex shapes [105]. Two types of phantoms were fabricated: mechanically homogeneous phantoms and phantoms comprising a hard inclusion (Young's modulus 450 MPa) in soft bulk (Young's modulus 23 kPa). The mechanical behavior of the silicones was measured independently using compression tests, providing stress-strain curves for each material from which moduli were estimated. Compression OCE was performed using a ring actuator setup as described previously [51]. A phase-sensitive technique [40] was used to measure sample displacement, and weighted least squares (WLS) strain estimation [53] was used to generate elastograms.

A linear elastic, axisymmetric 3D model was employed, and the phantom geometry and material behavior from the compression tests were used as inputs to the simulations. FEM produced simulations of sample displacement and strain fields, which were compared to that produced experimentally for validation. Once agreement was obtained between the measured and simulated displacements and strain, the simulated stress distributions could also be analyzed to aid interpretation of mechanical artifacts in the elastograms. Two prevalent sources of stress nonuniformity in the compression experiments are discussed here: friction and stress concentrations at feature boundaries.

*Friction:* For a homogeneous sample undergoing uniaxial compression, the strain and stress are expected to be uniform throughout the sample. For nearly incompressible materials such as soft tissues, axial compression is coupled to lateral expansion in order to conserve volume, as discussed in Sect. 32.2.4. If friction is present between the sample and the compressor, this restricts lateral motion of the sample at the boundary, resulting in lower strain, and, as a result, a region of apparently higher stiffness in the elastogram. To demonstrate the effect of friction on the resulting elastogram, two OCE measurements of a 0.8 mm thick, homogeneous silicone phantom were acquired with different boundary conditions. The results are shown in Fig. 32.20. In the first experiment, a lubricant was applied at both surfaces to allow slipping of the sample boundary against the compression plate. In the second, no lubricant was used on either surface. In the resulting elastograms shown in Fig. 32.20, the lubricated case shows a homogeneous strain field, as expected, while in the non-lubricated case, the effect of friction manifests as two bands of low strain at the top and bottom surfaces. These experiments were also simulated with FEM, using the two extreme boundary conditions of frictionless and no-slip at the surface, respectively. The representative plots (taken from the center of the sample) of displacement versus depth in Fig. 32.20 show good agreement between the measured and simulated displacements. This example demonstrates the importance of considering boundary conditions both when acquiring and interpreting elastograms in compression OCE.

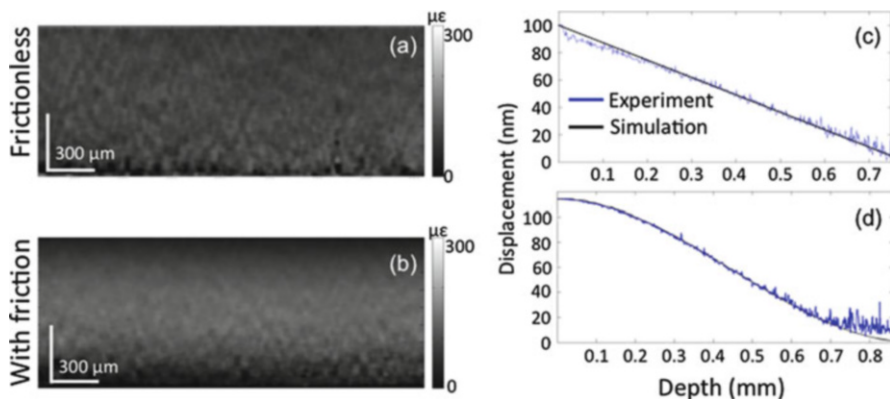


**Fig. 32.20** (a, b) Experimental strain elastograms and (c, d) comparison of measured and simulated displacement plots for the cases of (a) and (c) frictionless and (b) and (d) no-slip conditions at the boundaries

*Stress Concentrations at Feature Boundaries:* When a lesion of higher stiffness than that of the background is present, this creates a region of low strain in the elastogram, as expected. However, stress concentrations also arise above, below, and at the sides of the lesion, resulting in regions of higher strain at these locations. Thus, the assumption of stress uniformity does not hold for this geometry; if the strain image were interpreted directly as elasticity, the regions of higher strain about the inclusion would erroneously be interpreted as regions of low stiffness. The magnitude of this artifact increases for increasing modulus contrast between the lesion and the background material and also depends on the position in depth of the lesion. To demonstrate the presence of these artifacts and the nonuniform stress field for the case of a stiff lesion, compression OCE was performed on a soft phantom with a hard inclusion embedded. The resulting experimental elastogram, simulated strain, and simulated stress fields are shown in Fig. 32.21. The experimental and simulated strain both show the regions of higher and lower strain around the inclusion, and the simulated stress field allows analysis of where the stress uniformity assumption fails.

Although a linear elastic FEM was employed in this initial study, the silicone materials used exhibit nonlinear behavior, as do many tissues. This results in a nonlinear relationship between the strain introduced to the sample and the resulting strain contrast; i.e., the elastogram contrast changes as a function of stress on the sample. This was observed to cause discrepancies between the model, for which a single modulus value was assigned to each material, and the experiments, in which the effective stiffness of each material varied depending on the applied stress. Although tissue may be assumed to behave linearly at strains  $<0.1$  [22], remaining in this linear regime is not always feasible when performing elastography of tissue, as large local deformations are common in the body; e.g., arteries undergo physiological strains of up to 0.2 [93]. This highlights a need to employ more advanced models of tissue to enable more accurate construction of elastograms.

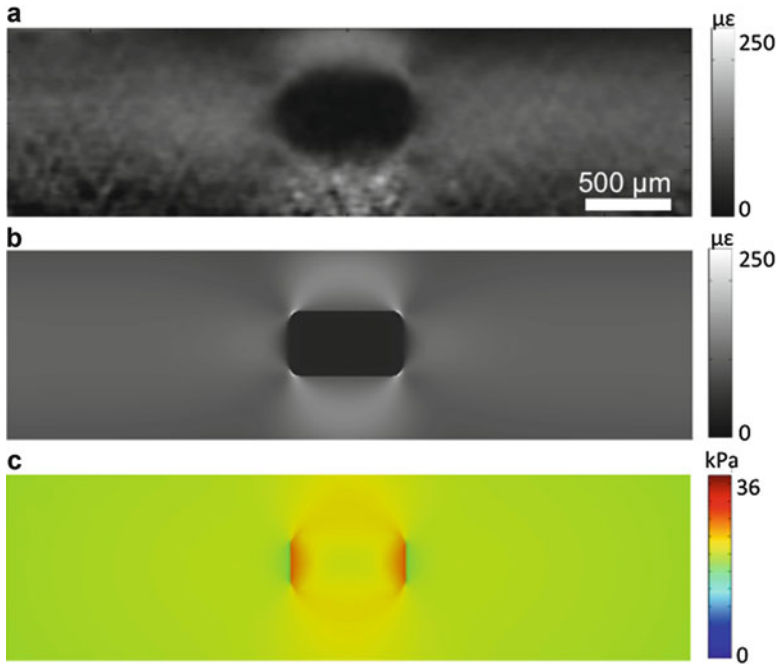
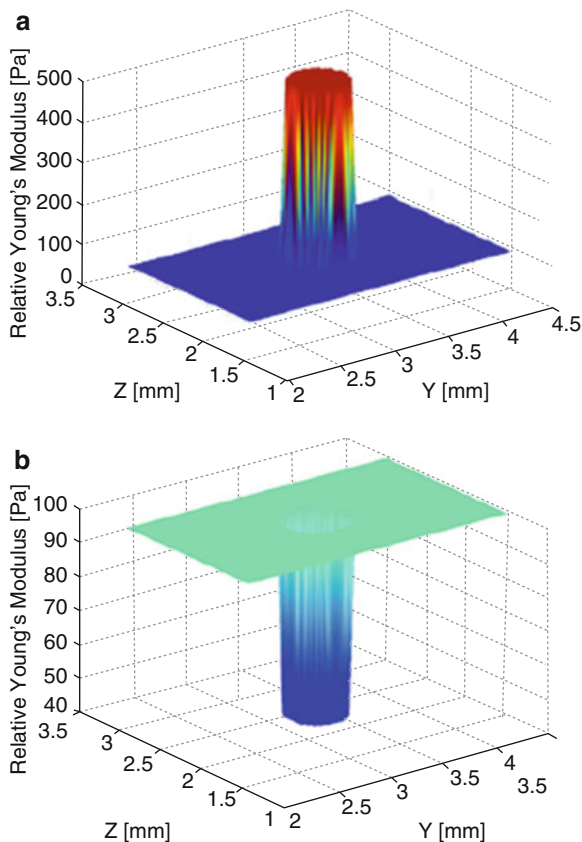


**Fig. 32.21** (a) Measured strain, (b) simulated strain, and (c) simulated stress of a phantom comprising a stiff inclusion in soft bulk, demonstrating regions of high strain due to stress concentrations about the inclusion

### 32.6.3 Model-Based Elastography: Inverse Methods for Quantitative Elastograms

As seen in the preceding example of compression elastography, elastograms constructed based on simplified models of tissue deformation do not always accurately represent tissue elasticity. In ultrasound and magnetic resonance elastography, several techniques have aimed to produce quantitative, reliable elastograms by approaching elastography as an inverse problem [106]. The forward problem in elastography can be formulated as follows: given a distribution of mechanical properties and boundary conditions, calculate the displacements resulting from an applied load, as described in Sect. 32.6.2. The inverse problem for elastography, then, attempts to calculate the distribution of mechanical properties from a distribution of measured displacements. Reconstructing elasticity images using inverse methods has been an active area of research in ultrasound and magnetic resonance elastography for several years [106], but only a few studies in OCE have begun to approach this problem. The earliest of these studies were toward the application of OCE for assessment of atherosclerotic plaque vulnerability [93, 107, 108]. These studies proposed an iterative approach to solving the inverse problem using FEM, in which the mechanical parameters in the model are optimized to produce the best match to

**Fig. 32.22** Estimated distribution of elasticity for (a) a hard inclusion in a soft bulk, simulating a calcified nodule in an artery wall, and (b) a soft inclusion in a stiffer bulk, simulating a lipid pool in an artery wall, as determined by an iterative solution to the inverse problem using simulated OCE data as an input to a finite element model of tissue (Modified from [108])



the measured displacements using OCT. Images of the resulting elasticity distributions for a hard and soft inclusion embedded in a bulk material of constant stiffness are shown in Fig. 32.22. These studies showed promising results in simulations of OCT-derived displacements of tissue, but would be very computationally intensive to implement and may be prone to error in the presence of experimental system noise.

Quantitative, model-based OCE has also been achieved by measuring sample response to a mechanical waveform, then fitting the measured response to an analytical model for motion in a viscoelastic material [52]. Although it provides quantitative maps of Young's modulus, this method requires solving the wave equation for each pixel, a computationally intensive and slow process. More recent studies have moved toward quantification of Young's modulus by implementing transient loading techniques in which the shear modulus may be extracted directly from the velocity of shear waves in the sample [23, 26, 56]. However, these quantitative techniques come at a loss of resolution, as they assume tissue homogeneity for the length over which shear wave speed is calculated [56, 57]. This assumption may not be suitable for imaging organs with heterogeneous, complex structures, such as the breast.

## 32.7 Outlook

Since its first demonstration in 1998, over 200 papers on OCE and related techniques have been published, accumulating over 500 citations in 2012 alone. As the technical development of OCT reaches maturity, the scope and capacity for the development of OCE is increasing. Indeed, over the last 2 years, the number of groups publishing in OCE has doubled. Comparison of the published literature suggests that OCE is at a similar stage of development to that of ultrasound elastography in the late 1990s, and thus, continued rapid development is expected in the coming years. In the following, we predict the key developments needed to enable the technique to flourish.

*Imaging Probes:* The majority of OCE results have been demonstrated on excised tissue when in vivo imaging is the intended application. However, the clinical applicability of many current implementations is limited. A key requirement is the development of probes incorporating both imaging optics and loading mechanisms. In recent years, as discussed in Sect. 32.5, this has been recognized, and an increasing number of OCE probe implementations have been proposed [19, 72, 98, 109]. This is a key enabling technology required for clinical OCE imaging, and substantial further work is required.

*Displacement Measurement:* Measurement of mechanical properties over a large range and with high sensitivity is ultimately limited by the measurable displacement. Using cross-correlation in speckle tracking, the dynamic range of measurable strain is limited to  $\sim 3.3$ . In phase-sensitive compression OCE, the measurable displacement range enables a strain dynamic range of  $>60$  and the minimum measurable displacement in phase-sensitive detection is in the sub-nanometer range [45]. In both speckle tracking and phase-sensitive methods, there is significant scope for improvement. In speckle tracking, there is a scope for parametric algorithms to provide sub-pixel displacement sensitivity, and in phase-sensitive methods, phase unwrapping algorithms will enable maximum displacements beyond the  $2\pi$  limit.

*Elastogram Fidelity:* Contrast in elastograms depends not only on the true elastic contrast within the tissue being probed but also on the accuracy of the employed mechanical model of tissue behavior. As illustrated in Sect. 32.6 for the particular case of compression OCE, erroneous assumptions about tissue mechanics, such as the assumption of uniform stress distribution, result in significant artifacts in elastograms, degrading their fidelity to the true underlying elastic properties. This and other common assumptions, such as that of linear elastic tissue behavior or tissue homogeneity over the acoustic wavelength in wave-based techniques, allow for straightforward estimation of the distribution of elastic properties and may in many cases prove sufficient for providing clinically useful contrast. However, the validity of employed assumptions must be assessed for each technique and proposed application. Finite element modeling is expected to remain an essential tool for validating the contrast generated using various OCE techniques and for analyzing how variables such as geometry, heterogeneity, boundary conditions, and loading rate impact on contrast.

*Applications:* Until now, the reported results of applying OCE to tissue have largely served to demonstrate a particular technique or implementation. In so doing,

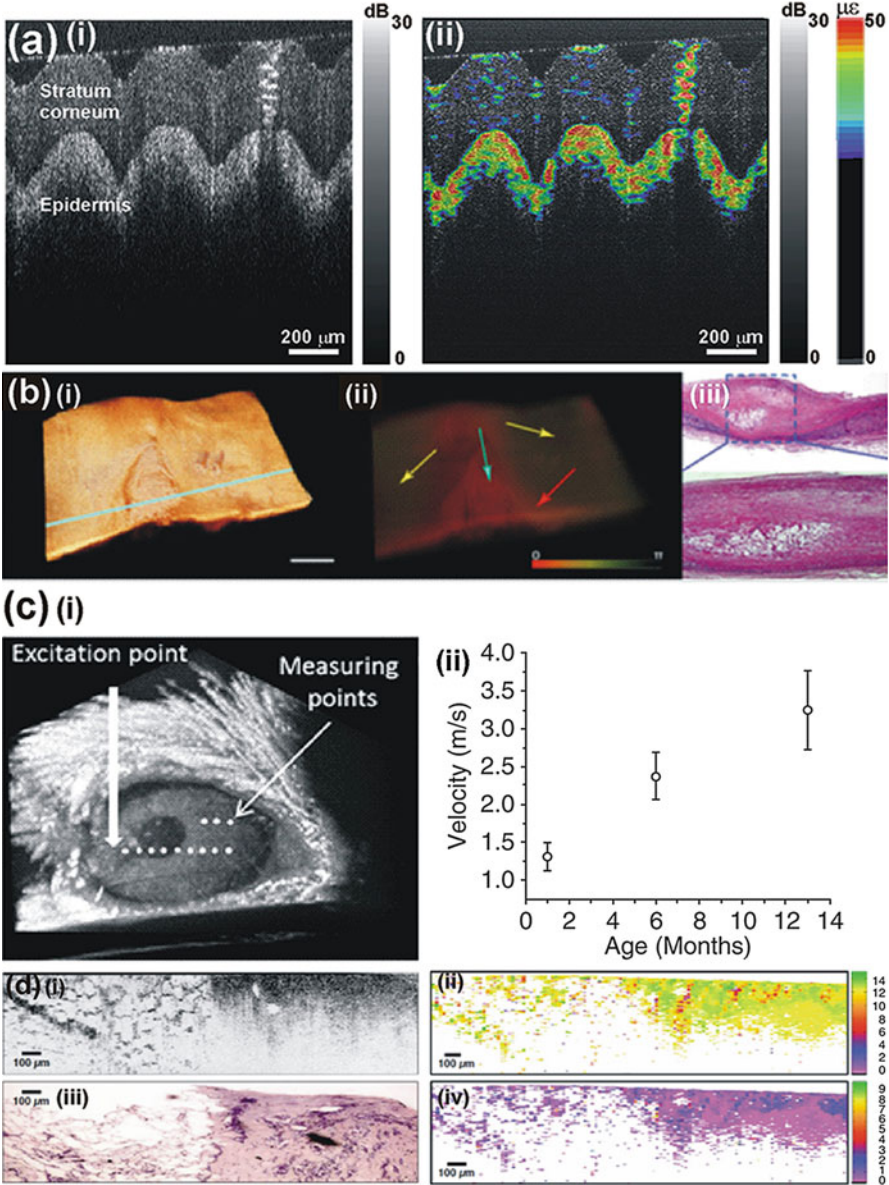


**Fig. 32.23** Example images from potential OCE clinical applications. (a) Dermatology, (Adapted from [51]), (b) cardiology [72], (c) ophthalmology [57], and (d) breast cancer [52]

such reports have highlighted a number of potential applications, including in dermatology (Fig. 32.23a) [11, 19, 24, 32, 51], cardiology (Fig. 32.23b) [30, 31, 72, 92, 107, 108, 110], ophthalmology (Fig. 32.23c) [57, 89, 90, 111], and breast cancer (Fig. 32.23d) [15, 52, 112]. As well as human in vivo applications, there is

opportunity for clinical *ex vivo* applications, e.g., as an intraoperative tumor margin assessment in freshly resected tumor masses and as a tool in studying animal models of disease.

Although various applications show promise or appear attractive, there is a need to *prove* the ability of OCE to provide additional contrast (particularly over standard OCT) through baseline *ex vivo* studies, co-registered with histology, of diseased and non-diseased tissue. To date, there have been no reports focused on the systematic application of OCE to multiple cases of a particular pathology. As discussed above, enabling such studies also depends on the further development of imaging probes.

OCE is undoubtedly at an early stage of development, especially when compared with the closely related fields of ultrasound and magnetic resonance elastography. The recent increase in activity in the field and the acceleration of progress suggest there is good cause to expect future clinical applications of this emerging technique.

*Note:* Since submitting this manuscript in April 2013, many works in this field, including our own, have been published. For a more recent review, see B. F. Kennedy et al., “A Review of Optical Coherence Elastography: Fundamentals, Techniques and Prospects” *IEEE J. Sel. Top. Quantum Electron.* 20, 7101217 (2014)

**Acknowledgments** BFK, KMK, and DDS acknowledge funding from the Australian Research Council, the National Health and Medical Research Council, the Raine Medical Research Foundation, and the University of Western Australia. They thank their colleagues and coworkers Prof Mark Bush, Mr Lixin Chin, Dr Chris Ford, and Dr Robert McLaughlin.

---

## References

1. Y.C. Fung, *Biomechanics: Mechanical Properties of Living Tissues* (Springer, New York, 1981)
2. K.J. Parker, M.M. Doyley, D.J. Rubens, Imaging the elastic properties of tissue: the 20 year perspective. *Phys. Med. Biol.* **56**, R1 (2011)
3. J. Ophir, I. Cespedes, H. Ponnekanti, Y. Yazdi, X. Li, Elastography: a quantitative method for imaging the elasticity of biological tissues. *Ultrason. Imaging* **13**, 111–134 (1991)
4. R. Muthupillai, D.J. Lomas, P.J. Rossman, J.F. Greenleaf, A. Manduca, R.L. Ehman, Magnetic resonance elastography by direct visualization of propagating acoustic strain waves. *Science* **269**, 1854–1857 (1995)
5. B.S. Garra, E.I. Cespedes, J. Ophir, S.R. Spratt, R.A. Zuurbier, C.M. Magnant, M.F. Pennanen, Elastography of breast lesions: initial clinical results. *Radiology* **202**, 79–86 (1997)
6. J. Foucher, E. Chanteloup, J. Vergniol, L. Castéra, B. Le Bail, X. Adhoute, J. Bertet, P. Couzigou, V. de Lédinghen, Diagnosis of cirrhosis by transient elastography (FibroScan): a prospective study. *Gut* **55**, 403–408 (2006)
7. D.L. Cochlin, R.H. Ganatra, D.F.R. Griffiths, Elastography in the detection of prostatic cancer. *Clin. Radiol.* **57**, 1014–1020 (2002)
8. S. Wojcinski, A. Farrok, S. Weber, A. Thomas, T. Fischer, T. Slowinski, W. Schmidand, F. Degenhardt, Multicenter study of ultrasound real-time tissue elastography in 779 cases for the assessment of breast lesions: improved diagnostic performance by combining the BI-RADS – US classification system with sonoelastography. *Ultraschall Med.* **31**, 484–491 (2010)
9. J.M. Schmitt, OCT elastography: imaging microscopic deformation and strain of tissue. *Opt. Express* **3**, 199–211 (1998)

10. D.D. Duncan, S.J. Kirkpatrick, Processing algorithms for tracking speckle shifts in optical elastography of biological tissues. *J. Biomed. Opt.* **6**, 418–426 (2001)
11. S.J. Kirkpatrick, R.K. Wang, D.D. Duncan, M. Kulesz-Martin, K. Lee, Imaging the mechanical stiffness of skin lesions by in vivo acousto-optical elastography. *Opt. Express* **14**, 9770–9779 (2006)
12. K. Daoudi, A.C. Boccara, E. Bossy, Detection and discrimination of optical absorption and shear stiffness at depth in tissue-mimicking phantoms by transient optoelastography. *Appl. Phys. Lett.* **94**, 154103 (2009)
13. D.S. Elson, R. Li, C. Dunsby, R. Eckersley, M.X. Tang, Ultrasound-mediated optical tomography: a review of current methods. *J. R. Soc. Interface Focus* **1**, 632–648 (2011)
14. S. Li, K.D. Mohan, W.W. Sanders, A.L. Oldenburg, Toward soft-tissue elastography using digital holography to monitor surface acoustic waves. *J. Biomed. Opt.* **16**, 116005–116005 (2011)
15. K.D. Mohan, A.L. Oldenburg, Elastography of soft materials and tissues by holographic imaging of surface acoustic waves. *Opt. Express* **20**, 18887–18897 (2012)
16. W. Michael Lai, D. Rubin, E. Krempf, *Introduction to Continuum Mechanics* (Butterworth-Heinemann, Oxford, 2010)
17. J.F. Greenleaf, M. Fatemi, M. Insana, Selected methods for imaging elastic properties of biological tissues. *Annu. Rev. Biomed. Eng.* **5**, 57–78 (2003)
18. K.J. Parker, L.S. Taylor, S. Gracowski, D.J. Rubens, A unified view of imaging the elastic properties of tissue. *J. Acoust. Soc. Am.* **117**, 2705–2712 (2005)
19. B.F. Kennedy, T.R. Hillman, R.A. McLaughlin, B.C. Quirk, D.D. Sampson, In vivo dynamic optical coherence elastography using a ring actuator. *Opt. Express* **17**, 21762–21772 (2009)
20. S.J. Kirkpatrick, D.D. Duncan, Optical assessment of tissue mechanics, in *Handbook of Optical Biomedical Diagnostics*, ed. by V.V. Tuchin (SPIE-The International Society for Optical Engineering, Bellingham, 2002), pp. 1037–1084
21. S. Abbas, B. Jonathan, L. Chris, B.P. Donald, Measuring the elastic modulus of ex vivo small tissue samples. *Phys. Med. Biol.* **48**, 2183 (2003)
22. T.A. Krouskop, T.M. Wheeler, F. Kallel, B.S. Garra, T. Hall, Elastic moduli of breast and prostate tissues under compression. *Ultrasound Imaging* **20**, 260–274 (1998)
23. X. Liang, M. Orescanin, K.S. Toohey, M.F. Insana, S.A. Boppart, Acoustomotive optical coherence elastography for measuring material mechanical properties. *Opt. Lett.* **34**, 2894–2896 (2009)
24. X. Liang, S.A. Boppart, Biomechanical properties of in vivo human skin from dynamic optical coherence elastography. *IEEE Trans. Biomed. Eng.* **57**, 953–959 (2010)
25. R. Manapuram, S. Aglyamov, F.M. Menodiado, M. Mashiatulla, S. Wang, S.A. Baranov, J. Li, S. Emelianov, K.V. Larin, Estimation of shear wave velocity in gelatin phantoms utilizing PhS-SSOCT. *Laser Phys.* **22**, 1439–1444 (2012)
26. M. Razani, A. Mariampillai, C. Sun, T.W.H. Luk, V.X.D. Yang, M.C. Kolios, Feasibility of optical coherence elastography measurements of shear wave propagation in homogeneous tissue equivalent phantoms. *Biomed. Opt. Express* **3**, 972–980 (2012)
27. A. Curatolo, B.F. Kennedy, D.D. Sampson, T.R. Hillman, Speckle in optical coherence tomography, in *Advanced Biophotonics: Tissue Optical Sectioning*, ed. by R.K. Wang, V.V. Tuchin (Taylor & Francis, London, 2013)
28. E. Archibald, A.E. Ennos, P.A. Taylor, A laser speckle interferometer for the detection of surface movements and vibrations, in *Optical Instruments and Techniques*, ed. by J.H. Dickson (Oriel, Newcastle upon Tyne, 1969), p. 265
29. J.A. Leendertz, Interferometric displacement measurement on scattering surfaces utilizing speckle effect. *J. Phys. E Sci. Instrum.* **3**, 214 (1970)
30. R. Chan, A. Chau, W. Karl, S. Nadkarni, A. Khalil, N. Iftimia, M. Shishkov, G. Tearney, M. Kaazempur-Mofrad, B. Bouma, OCT-based arterial elastography: robust estimation exploiting tissue biomechanics. *Opt. Express* **12**, 4558–4572 (2004)

31. J. Rogowska, N. Patel, J. Fujimoto, M. Brezinski, Optical coherence tomographic elastography technique for measuring deformation and strain of atherosclerotic tissues. *Heart* **90**, 556–562 (2004)
32. F.M. Hendriks, D. Brokken, C.W. Oomens, D.L. Bader, F.P. Baaijens, The relative contributions of different skin layers to the mechanical behavior of human skin in vivo using suction experiments. *Med. Eng. Phys.* **28**, 259–266 (2006)
33. S.J. Kirkpatrick, R.K. Wang, D.D. Duncan, OCT-based elastography for large and small deformations. *Opt. Express* **14**, 11585–11597 (2006)
34. H.J. Ko, W. Tan, R. Stack, S.A. Boppart, Optical coherence elastography of engineered and developing tissue. *Tissue Eng.* **12**, 63–73 (2006)
35. D. Duncan, S. Kirkpatrick, Performance analysis of a maximum-likelihood speckle motion estimator. *Opt. Express* **10**, 927–941 (2002)
36. B.F. Kennedy, T.R. Hillman, A. Curatolo, D.D. Sampson, Speckle reduction in optical coherence tomography by strain compounding. *Opt. Lett.* **35**, 2445–2447 (2010)
37. J. Meunier, Tissue motion assessment from 3D echographic speckle tracking. *Phys. Med. Biol.* **43**, 1241 (1998)
38. S. Gahagnon, Y. Mofid, G. Josse, F. Ossant, Skin anisotropy in vivo and initial natural stress effect: a quantitative study using high-frequency static elastography. *J. Biomech.* **45**, 2860–2865 (2012)
39. J.-L. Gennisson, S. Catheline, S. Chaffai, M. Fink, Transient elastography in anisotropic medium: application to the measurement of slow and fast shear wave speeds in muscles. *J. Acoust. Soc. Am.* **114**, 536–541 (2003)
40. R.K. Wang, Z. Ma, S.J. Kirkpatrick, Tissue Doppler optical coherence elastography for real time strain rate and strain mapping of soft tissue. *Appl. Phys. Lett.* **89**, 144103-144103-144103 (2006)
41. R.K. Wang, S. Kirkpatrick, M. Hinds, Phase-sensitive optical coherence elastography for mapping tissue microstrains in real time. *Appl. Phys. Lett.* **90**, 164105 (2007)
42. Y. Zhao, Z. Chen, C. Saxer, S. Xiang, J.F. de Boer, J.S. Nelson, Phase-resolved optical coherence tomography and optical Doppler tomography for imaging blood flow in human skin with fast scanning speed and high velocity sensitivity. *Opt. Lett.* **25**, 114–116 (2000)
43. J.W. Goodman, *Statistical Optics* (Wiley, New York, 1985)
44. B. Park, M.C. Pierce, B. Cense, S.-H. Yun, M. Mujat, G. Tearney, B. Bouma, J. de Boer, Real-time fiber-based multi-functional spectral-domain optical coherence tomography at 1.3  $\mu\text{m}$ . *Opt. Express* **13**, 3931–3944 (2005)
45. R.K. Wang, A.L. Nuttall, Phase-sensitive optical coherence tomography imaging of the tissue motion within the organ of Corti at a subnanometer scale: a preliminary study. *J. Biomed. Opt.* **15**, 056005–056005 (2010)
46. X. Liang, S.G. Adie, R. John, S.A. Boppart, Dynamic spectral-domain optical coherence elastography for tissue characterization. *Opt. Express* **18**, 14183–14190 (2010)
47. B.F. Kennedy, M. Wojtkowski, M. Szkulmowski, K.M. Kennedy, K. Karnowski, D.D. Sampson, Improved measurement of vibration amplitude in dynamic optical coherence elastography. *Biomed. Opt. Express* **3**, 3138–3152 (2012)
48. M. Szkulmowski, A. Szkulmowska, T. Bajraszewski, A. Kowalczyk, M. Wojtkowski, Flow velocity estimation using joint spectral and time domain optical coherence tomography. *Opt. Express* **16**, 6008–6025 (2008)
49. S.G. Adie, B.F. Kennedy, J.J. Armstrong, S.A. Alexandrov, D.D. Sampson, Audio frequency in vivo optical coherence elastography. *Phys. Med. Biol.* **54**, 3129 (2009)
50. S.-R. Huang, R.M. Lerner, K.J. Parker, On estimating the amplitude of harmonic vibration from the Doppler spectrum of reflected signals. *J. Acoust. Soc. Am.* **88**, 2702–2712 (1990)
51. B.F. Kennedy, X. Liang, S.G. Adie, D.K. Gerstmann, B.C. Quirk, S.A. Boppart, D.D. Sampson, In vivo three-dimensional optical coherence elastography. *Opt. Express* **19**, 6623–6634 (2011)
52. X. Liang, A.L. Oldenburg, V. Crecea, E.J. Chaney, S.A. Boppart, Optical micro-scale mapping of dynamic biomechanical tissue properties. *Opt. Express* **16**, 11052–11065 (2008)

53. B.F. Kennedy, S.H. Koh, R.A. McLaughlin, K.M. Kennedy, P.R.T. Munro, D.D. Sampson, Strain estimation in phase-sensitive optical coherence elastography. *Biomed. Opt. Express* **3**, 1865–1879 (2012)
54. C. Li, G. Guan, R. Reif, Z. Huang, R.K. Wang, Determining elastic properties of skin by measuring surface waves from an impulse mechanical stimulus using phase-sensitive optical coherence tomography. *J. R. Soc. Interface* **9**, 831–841 (2011)
55. C. Li, Z. Huang, R.K. Wang, Elastic properties of soft tissue-mimicking phantoms assessed by combined use of laser ultrasonics and low coherence interferometry. *Opt. Express* **19**, 10153–10163 (2011)
56. C. Li, G. Guan, X. Cheng, Z. Huang, R.K. Wang, Quantitative elastography provided by surface acoustic waves measured by phase-sensitive optical coherence tomography. *Opt. Lett.* **37**, 722–724 (2012)
57. R.K. Manapuram, S.R. Aglyamov, F.M. Monediado, M. Mashiattulla, J. Li, S.Y. Emelianov, K.V. Larin, In vivo estimation of elastic wave parameters using phase-stabilized swept source optical coherence elastography. *J. Biomed. Opt.* **17**, 100501–100501 (2012)
58. M. del Socorro Hernández-Montes, C. Furlong, J.J. Rosowski, N. Hulli, E. Harrington, J.T. Cheng, M.E. Ravicz, F.M. Santoyo, Optoelectronic holographic otoscope for measurement of nano-displacements in tympanic membranes. *J. Biomed. Opt.* **14**, 034023–034023 (2009)
59. M. Leclercq, M. Karray, V. Isnard, F. Gautier, P. Picart, Quantitative evaluation of skin vibration induced by a bone-conduction device using holographic recording in a quasi-time-averaging regime, in *Digital Holography and Three-Dimensional Imaging* (Optical Society of America, 2012), paper DW1C
60. G. Eskin, J. Ralston, On the inverse boundary value problem for linear isotropic elasticity. *Inverse Probl.* **18**, 907 (2002)
61. B.A. Auld, General electromechanical reciprocity relations applied to the calculation of elastic wave scattering coefficients. *Wave Motion* **1**, 3–10 (1979)
62. E.R. Engdahl, R. van der Hilst, R. Buland, Global teleseismic earthquake relocation with improved travel times and procedures for depth determination. *Bull. Seismol. Soc. Am.* **88**, 722–743 (1998)
63. F.-C. Lin, M.P. Moschetti, M.H. Ritzwoller, Surface wave tomography of the western United States from ambient seismic noise: Rayleigh and Love wave phase velocity maps. *Geophys. J. Int.* **173**, 281–298 (2008)
64. T.J. Royston, H.A. Mansy, R.H. Sandler, Excitation and propagation of surface waves on a viscoelastic half-space with application to medical diagnosis. *J. Acoust. Soc. Am.* **106**, 3678–3686 (1999)
65. X. Zhang, J.F. Greenleaf, Estimation of tissue's elasticity with surface wave speed. *J. Acoust. Soc. Am.* **122**, 2522–2525 (2007)
66. G. Pedrini, S. Schedin, H.J. Tiziani, Pulsed digital holography combined with laser vibrometry for 3D measurements of vibrating objects. *Opt. Lasers Eng.* **38**, 117–129 (2002)
67. L. Mertz, Real-time fringe-pattern analysis. *Appl. Opt.* **22**, 1535–1539 (1983)
68. K.R. Nightingale, M.L. Palmeri, R.W. Nightingale, G.E. Trahey, On the feasibility of remote palpation using acoustic radiation force. *J. Acoust. Soc. Am.* **110**, 625–634 (2001)
69. Y. Takuma, K. Nouse, Y. Morimoto, J. Tomokuni, A. Sahara, N. Toshikuni, H. Takabatake, H. Shimomura, A. Doi, I. Sakakibara, K. Matsueda, H. Yamamoto, Measurement of spleen stiffness by acoustic radiation force impulse imaging identifies cirrhotic patients with esophageal varices. *Gastroenterology* **144**, 92–101 (2013)
70. [http://www.medical.siemens.com/webapp/wcs/stores/servlet/PSGenericDisplay~q\\_catalogId~e\\_1~a\\_langId~e\\_1~a\\_pageId~e\\_110950~a\\_storeId~e\\_10001.htm](http://www.medical.siemens.com/webapp/wcs/stores/servlet/PSGenericDisplay~q_catalogId~e_1~a_langId~e_1~a_pageId~e_110950~a_storeId~e_10001.htm)
71. G. van Soest, R. R. Bouchard, F. Mastik, N. de Jong, A. F. W. van der Steen, Robust intravascular optical coherence elastography driven by acoustic radiation pressure, in *Optical Coherence Tomography and Coherence Techniques III* (Optical Society of America, 2007), paper 66270EE

72. W. Qi, R. Chen, L. Chou, G. Liu, J. Zhang, Q. Zhou, Z. Chen, Phase-resolved acoustic radiation force optical coherence elastography. *J. Biomed. Opt.* **17**, 110505–110505 (2012)
73. E. Bossy, A.R. Funke, K. Daoudi, A.-C. Boccara, M. Tanter, M. Fink, Transient optoelastography in optically diffusive media. *Appl. Phys. Lett.* **90**, 174111–174113 (2007)
74. V. Crecea, A.L. Oldenburg, X. Liang, T.S. Ralston, S.A. Boppart, Magnetomotive nanoparticle transducers for optical rheology of viscoelastic materials. *Opt. Express* **17**, 23114–23122 (2009)
75. A.L. Oldenburg, S.A. Boppart, Resonant acoustic spectroscopy of soft tissues using embedded magnetomotive nanotransducers and optical coherence tomography. *Phys. Med. Biol.* **55**, 1189–1201 (2010)
76. A.L. Oldenburg, F.J.J. Toublan, K.S. Suslick, A. Wei, S.A. Boppart, Magnetomotive contrast for in vivo optical coherence tomography. *Opt. Express* **13**, 6597–6614 (2005)
77. A. Grimwood, L. Garcia, J. Bamber, J. Holmes, P. Woolliams, P. Tomlins, Q.A. Pankhurst, Elastographic contrast generation in optical coherence tomography from a localized shear stress. *Phys. Med. Biol.* **55**, 5515 (2010)
78. A.L. Oldenburg, G. Wu, D. Spivak, F. Tsui, A.S. Wolberg, T.H. Fischer, Imaging and elastometry of blood clots using magnetomotive optical coherence tomography and labeled platelets. *IEEE J. Sel. Top. Quantum Electron.* **18**, 1100–1121 (2012)
79. R. John, E.J. Chaney, S.A. Boppart, Dynamics of magnetic nanoparticle-based contrast agents in tissues tracked using magnetomotive optical coherence tomography. *IEEE J. Sel. Top. Quantum Electron.* **16**, 691–697 (2010)
80. J. Kim, A. Ahmad, S.A. Boppart, Dual-coil magnetomotive optical coherence tomography for contrast enhancement in liquids. *Opt. Express* **21**, 7139–7147 (2013)
81. M. Fatemi, J.F. Greenleaf, Ultrasound-stimulated vibro-acoustic spectrography. *Science* **280**, 82–85 (1998)
82. M. Fatemi, J.F. Greenleaf, Vibro-acoustography: an imaging modality based on ultrasound-stimulated acoustic emission. *Proc. Natl. Acad. Sci. U. S. A.* **96**, 6603–6608 (1999)
83. M.W. Urban, A. Alizad, W. Aquino, J.F. Greenleaf, M. Fatemi, A review of vibro-acoustography and its applications in medicine. *Curr. Med. Imaging Rev.* **7**, 350–359 (2011)
84. J. Greenleaf, M. Fatemi, Vibro-acoustography: speckle free ultrasonic imaging. *Med. Phys.* **34**, 2527–2528 (2007)
85. J.F. Greenleaf, M. Fatemi, M. Belohlavek, Ultrasound stimulated vibro-acoustography. *Lect. Notes Comput. Sci.* **3117**, 1–10 (2004)
86. M. Fatemi, L.E. Wold, A. Alizad, J.F. Greenleaf, Vibro-acoustic tissue mammography. *IEEE Trans. Med. Imaging* **21**, 1–8 (2002)
87. S.G. Adie, X. Liang, B.F. Kennedy, R. John, D.D. Sampson, S.A. Boppart, Spectroscopic optical coherence elastography. *Opt. Express* **18**, 25519–25534 (2010)
88. C. Li, G. Guan, Z. Huang, M. Johnstone, R.K. Wang, Noncontact all-optical measurement of corneal elasticity. *Opt. Lett.* **37**, 1625–1627 (2012)
89. D. Alonso-Caneiro, K. Karnowski, B.J. Kaluzny, A. Kowalczyk, M. Wojtkowski, Assessment of corneal dynamics with high-speed swept source optical coherence tomography combined with an air puff system. *Opt. Express* **19**, 14188–14199 (2011)
90. S. Wang, J. Li, R.K. Manapuram, F.M. Menodiado, D.R. Ingram, M.D. Twa, A.J. Lazar, D.C. Lev, R.E. Pollock, K.V. Larin, Noncontact measurement of elasticity for the detection of soft-tissue tumors using phase-sensitive optical coherence tomography combined with a focused air-puff system. *Opt. Lett.* **37**, 5184–5186 (2012)
91. J.P. Williamson, R.A. McLaughlin, W.J. Noffsinger, A.L. James, V.A. Baker, A. Curatolo, J.J. Armstrong, A. Regli, K.L. Shepherd, G.B. Marks, Elastic properties of the central airways in obstructive lung diseases measured using anatomical optical coherence tomography. *Am. J. Respir. Crit. Care Med.* **183**, 612–619 (2011)
92. A. Chau, R. Chan, M. Shishkov, B. MacNeill, N. Iftimia, G. Tearney, R. Kamm, B. Bouma, M. Kaazempur-Mofrad, Mechanical analysis of atherosclerotic plaques based on optical coherence tomography. *Ann. Biomed. Eng.* **32**, 1494–1503 (2004)

93. R. Karimi, T. Zhu, B.E. Bouma, M.R. Kaazempur Mofrad, Estimation of nonlinear mechanical properties of vascular tissues via elastography. *Cardiovasc. Eng.* **8**, 191–202 (2008)
94. J. Yin, H.C. Yang, X. Li, J. Zhang, Q. Zhou, C. Hu, K.K. Shung, Z. Chen, Integrated intravascular optical coherence tomography ultrasound imaging system. *J. Biomed. Opt.* **15**, 010512 (2010)
95. J. Sliwa, Y. Liu, *Optical coherence tomography catheter for elastographic property mapping of lumens utilizing micropalpation*, U.S. Patent 20,120,265,062, 2012
96. X. Li, C. Chudoba, T. Ko, C. Pitris, J.G. Fujimoto, Imaging needle for optical coherence tomography. *Opt. Lett.* **25**, 1520–1522 (2000)
97. R.A. McLaughlin, B.C. Quirk, A. Curatolo, R.W. Kirk, L. Scolaro, D. Lorensen, P. Robbins, B. Wood, C. Saunders, D. Sampson, Imaging of breast cancer with optical coherence tomography needle probes: feasibility and initial results. *IEEE J. Sel. Top. Quantum Electron.* **18**, 1184–1191 (2012)
98. K.M. Kennedy, B.F. Kennedy, R.A. McLaughlin, D.D. Sampson, Needle optical coherence elastography for tissue boundary detection. *Opt. Lett.* **37**, 2310–2312 (2012)
99. O.A. Shergold, N.A. Fleck, Experimental investigation into the deep penetration of soft solids by sharp and blunt punches, with application to the piercing of skin. *J. Biomech. Eng. – T. ASME* **127**, 838 (2005)
100. C. Li, S. Li, G. Guan, C. Wei, Z. Huang, R.K. Wang, A comparison of laser ultrasound measurements and finite element simulations for evaluating the elastic properties of tissue mimicking phantoms. *Opt. Laser Technol.* **44**, 866–871 (2012)
101. M. Bilgen, Target detectability in acoustic elastography. *IEEE T. Ultrason. Ferroelectr.* **46**, 1128–1133 (1999)
102. F. Kallel, M. Bertrand, J. Ophir, Fundamental limitations on the contrast-transfer efficiency in elastography: an analytic study. *Ultrasound Med. Biol.* **22**, 463–470 (1996)
103. H. Ponnekanti, J. Ophir, Y. Huang, I. Cespedes, Fundamental mechanical limitations on the visualization of elasticity contrast in elastography. *Ultrasound Med. Biol.* **21**, 533–543 (1995)
104. T. Varghese, J. Ophir, An analysis of elastographic contrast-to-noise ratio. *Ultrasound Med. Biol.* **24**, 915–924 (1998)
105. G. Lamouche, B.F. Kennedy, K.M. Kennedy, C.-E. Bisailon, A. Curatolo, G. Campbell, V. Pazos, D.D. Sampson, Review of tissue simulating phantoms with controllable optical, mechanical and structural properties for use in optical coherence tomography. *Biomed. Opt. Express* **3**, 1381–1398 (2012)
106. M. Doyley, Model-based elastography: a survey of approaches to the inverse elasticity problem. *Phys. Med. Biol.* **57**, R35 (2012)
107. A.H. Chau, R.C. Chan, M. Shishkov, B. MacNeill, N. Iftimia, G.J. Tearney, R.D. Kamm, B.E. Bouma, M.R. Kaazempur-Mofrad, Mechanical analysis of atherosclerotic plaques based on optical coherence tomography. *Ann. Biomed. Eng.* **32**, 1494–1503 (2004)
108. A.S. Khalil, R.C. Chan, A.H. Chau, B.E. Bouma, M.R.K. Mofrad, Tissue elasticity estimation with optical coherence elastography: toward mechanical characterization of in vivo soft tissue. *Ann. Biomed. Eng.* **33**, 1631–1639 (2005)
109. L.M. Peterson, M.W. Jenkins, S. Gu, L. Barwick, M. Watanabe, A.M. Rollins, 4D shear stress maps of the developing heart using Doppler optical coherence tomography. *Biomed. Opt. Express* **3**, 3022–3032 (2012)
110. G. van Soest, F. Mastik, N. de Jong, A.F.W. van der Steen, Robust intravascular optical coherence elastography by line correlations. *Phys. Med. Biol.* **52**, 2445 (2007)
111. M.R. Ford, J.W.J. Dupps, A.M. Rollins, A.S. Roy, Z. Hu, Method for optical coherence elastography of the cornea. *J. Biomed. Opt.* **16**, 016005–016005 (2011)
112. A. Srivastava, Y. Verma, K.D. Rao, P.K. Gupta, Determination of elastic properties of resected human breast tissue samples using optical coherence tomographic elastography. *Strain* **47**, 75–87 (2011)